Depth dependent optical and elasto-optical effects of ion implantation studied by time-domain Brillouin scattering

By

Andrey Baydin

Dissertation

Submitted to the Faculty of the

Graduate School of Vanderbilt University

in partial fulfillment of the requirements

for the degree of

DOCTOR OF PHILOSOPHY

in

Physics

May 11, 2018

Nashville, Tennessee

Approved:

Norman H. Tolk, Ph.D.

Leonard C. Feldman, Ph.D.

Jimmy L. Davidson, Ph.D.

Sokrates T. Pantelides, Ph.D.

David J. Ernst, Ph.D.

Kirill I. Bolotin, Ph.D.

ACKNOWLEDGMENTS

First of all, I would like to thank my advisor Norman Tolk for his vision, support and mentoring style. I thank my PhD committee members; Dr. Leonard Feldman, Dr. Jimmy Davidson, Dr. Sokrates Pantelides, Dr. Kirill Bolotin and Dr. David Ernst for our research related conversations and their suggestions. Special thanks to my friends and co-workers including but not limited to Dr. Halina Krzyzanowska, Dr. Joy Garnett, Dr. Stephanie Gilbert-Corder, Dr. Jennifer Jones, Dr. Andrey Klots, Rustam Gatamov and many others who have contributed to my research progress and made this process enjoyable. I would also like to thank VINSE staff: Anthony Hmelo, Bo Choi, Ben Schmidt, Dmitry Koktysh and Department of Physics and Astronomy administrative team: Don Pickert, Peggy McGowan, Barbara Amann, Sheila Warf and Libby Johnson for their support. I thank my parents for their effort and support through all my education.

Above all, to my amazing wife Darya and my children: thank you for your patience, support, and love.

TABLE OF CONTENTS

Page

LIST OF TABLES

LIST OF FIGURES

Chapter 1

Introduction

1.1 Motivation

Defects, the origin of disorder, can be introduced into a specimen in various ways, e.g. during either materials growth, device fabrication processes or operation in harsh environments. Determining specifics of the relationship between structural disorder and basic optical properties, such as the complex refractive index and the photoelastic coefficients, is the key to understand the behavior of materials that have some amount of disorder.

Ion implantation is widely used for functionalizing and modifying materials. Using this method, many materials properties can be tailored to determine desired morphological [6, 7], mechanical [8, 9], electronic (doping), and optical properties [1]. In addition, ion implantation in conjunction with thermal processing can be used to form smart and active ceramic nanocomposite surfaces by embedding nanophase precipitates of metal-insulator transition [10, 11] or ferromagnetic [12, 13] materials in inactive hosts.

One of the main building blocks of quantum information processing and communication is solid-state single-photon emitters. The development of light sources that produce photons with controllable quantum correlations is a major part of quantum photonics research. Single photon emitters are being studied in different solid-state material systems such as color centers in crystals, defect states in two-dimensional materials, and quantum dots. Of these complexes, the NV^- center in diamond is the most studied [14, 15, 16]. Recently, it has been recognized that isolated defects in silicon carbide can serve as long-

lifetime atomic like states suitable for coherent single photon generation and possibly quantum computing structures [17, 18, 19]. Silicon carbide based single-photon sources are ultrabright, operate at room-temperature, and are photostable in a device-friendly material [19]. Isolated electron spins in silicon carbide that can be addressed optically exhibit coherence times of more than a millisecond [17] . These properties make silicon carbide an ideal candidate for atomic-scale spintronics and quantum information technology.

Further advancement in fabrication quantum devices based on solid-state qubits is limited by difficulties in exact placement of defect based qubits. Ion implantation is a standard tool of the semiconductor industry and is eminently suitable to address this challenge. Deterministic doping by single ion implantation and the precise placement of individual dopant atoms into devices is currently being pursued [20]. A remarkable range of controlled quantum phenomena in phosphorus implanted silicon devices has been demonstrated. There are still challenges to build a device with an array of deterministically implanted atoms. However, the development of ion implantation techniques is approaching sub-10 nm range localization which is required for large scale devices [21, 22, 23, 24].

Overall, understanding ion-matter interaction such as defect creation and defect dynamics during ion implantation as well as the damage produced by ion implantation are of great importance to many different applications and, particularly, to the emerging filed of quantum information technology.

1.2 Statement of work

In this thesis, time domain Brillouin scattering (TDBS) is applied to study depth dependent optical and elasto-optical effects of ion implantation in silicon carbide and gallium arsenide. TDBS, also known as picosecond ultrasonics or coherent acoustic phonon (CAP) spectroscopy, is a subset of the more general category of ultrafast pump-and-probe experiments. When a strong ultrafast ($<$1 ps) optical pump pulse is incident on a surface of opaque material, it generates a traveling CAP wave (or strain wave) due to inhomogeneous pump light absorption. The CAP wave locally perturbs the refractive index as it traverses the material. Thus, when a optical probe pulse is incident on a sample at a delayed time its reflection or transmission is modulated by the CAP wave. Interference of probe light waves reflected from the surface of the material and the traveling CAP wave results in an oscillatory time dependent reflectivity/transmissivity signal (Brillouin oscillations). Amplitude, decay and frequency of Brillouin oscillations are highly sensitive to optical and elastic material properties. For example, by analyzing Brillouin oscillation, the complex refractive index (see Chapter 4) and the photoelastic coefficient (see Chapter 5) as function of depth can be obtained.

To date, TDBS has been widely used to access depth dependent material properties such as elastic and optical inhomogeneities in disordered films [25, 26, 27], ion implantation induced modification of interfacial bonding [28], sub-m textures in materials compressed at megabar pressures [29, 30], doping profiles [31], distribution of stress [32], imaging of grain microstructure [33], and determination of laser-induced temperature gradients in liquids [34]. It has been shown that TDBS is sensitive to ion implantation induced damage

in gallium arsenide [35, 5] and diamond [36] at low fluences. Thus, the application of TDBS to study ion matter interactions is advantageous and further development of TDBS to access single defects is important and promising for quantum information technology in terms of qubit positioning and linking qubits with sound [37].

1.3 Thesis outline

This thesis is structured as follows:

Chapter 2 starts with an introduction to ion implantation, its advantages and a discussion of the basic physics of the ion matter interaction. Ion ranges and depth dependent damage profiles with an explanation of analytical models to fit depth profiles and ab-initio software, SRIM/TRIM, used for prediction of ion ranges and damage cascades, are included.

Chapter 3 explains different aspects of time domain Brillouin scattering, i.e. strain wave generation and propagation. It also introduces and develops a theoretical model that will be use in the following chapters to analyze the experimental data. At the end of this chapter, a novel method for measuring acoustic deformation potentials as a function of energy is proposed and demonstrated for gallium phosphide crystal.

Chapter 4 reports on depth and defect density dependence of the complex refractive index of n-type 4H-SiC arising from 180 keV hydrogen ion implantation at several fluences. It is shown that the extinction coefficient of silicon carbide increases linearly with vacancy concentration, whereas the refractive index has nonlinear dependence. In terms of depth dependent profiles, the implantation-induced change in the refractive index profile is broader and skewed more to the surface side than the vacancy/defect profile predicted by

the TRIM code (Monte Carlo calculations). We postulate that the observed increase in the refractive index is due to contributions from the atomic bond polarizability and/or structure factor, which means that the ionization from electronic stopping is likely to be a major contributing factor leading to an increase in the refractive index. These results add one more significant point to the body of data that relates the large change in the index of refraction to the atomic bond polarizability with ion bombardment for covalent semiconductors.

In Chapter 5 measurements of the photoelastic coefficient of hydrogen implanted gallium arsenide are discussed. First, it is shown analytically that the observed changes in the amplitude of Brillouin oscillations in damaged gallium arsenide are related to the depth dependent photoelastic coefficient. Then, the derived formulas are used to extract the depth and defect density dependence of photoelastic coefficient of gallium arsenide. The measured depth-dependent profiles are found to be broader than the defect distribution profiles predicted by Monte Carlo simulations. This fact indicates that the changes in photoelastic coefficient depend nonlinearly on the defect concentrations created by the hydrogen implantation. These studies provide insight into the spatial extent to which defects influence photoelastic properties of GaAs.

Chapter 6 summarizes the thesis and provides some future directions and experiments as an extension of the current study.

Chapter 2

Ion implantation

Ion implantation is the process of accelerating ions of a particular chemical element into a solid target that changes the physical, chemical, or electrical properties of the target. Ion implantation is widely used for functionalizing and modifying materials. Using this method, many materials properties can be tailored to determine desired morphological [6, 7], mechanical [8, 9], electronic (doping), and optical properties [1]. In addition, ion implantation in conjunction with thermal processing can be used to form smart and active ceramic nanocomposite layers by embedding nanophase precipitates of metal-insulator-transition [10, 11] or ferromagnetic [12, 13] materials in inactive hosts. Further development of ion implantation for localization precision and deterministic doping promises to make quantum technology a practical reality [20, 21, 22, 23, 24].

The topics covered in this chapter include review of electronic and nuclear stopping, characterization of ion and damage profiles by analytic methods, prediction of ion ranges and damage associated with by Monte Carlo calculations, and finally, channeling phenomena.

2.1 Review of material properties affected by ion implantation

Ion implantation primarily modifies near surface layers on a micrometer scale. There are many materials properties and applications that are affected by surface/near surface modification. They are summarized in Table 2.1. Ion implantation along with coating

deposition and diffusion of impurities provides highly controllable way to effect surface/-subsurface modification.

Table 2.1: Properties influenced by surface features [1]

Mechanical	Chemical	Electrical	Optical
Microhardness	Corrosion	Resistivity	Color
Friction	Passivation	Photoconductivity	Reflectivity
Adhesion	Diffusion	Electron mobility	Transmission
Wear	Reactivity	Semiconductivity	Optoelectronics

Another big application of ion implantation processing is the computer chips production because it offers room temperature operation for dopant implantation in precisely defined regions with fewer thermal cycles. Table 2.2 describes the advantages and disadvantages of using ion implantation as a doping method for semiconductors in contrast to diffusion doping.

From the optical device point of view ion implantation can effectively serve as a tool to fabricate anti-reflection coatings, wavelength selective mirrors, bandpass filters, waveguides and so on [1].

2.2 Ion ranges and damage

Upon entering the substrate, implanted ions loose energy due to nuclear and electronic stopping. Figure 2.1 shows a schematic diagram of ion stopping mechanisms. During nuclear stopping, energy is transferred from the energetic ion to the target (Si, for example) nuclei. If the energetic ion has sufficient energy, it may displace a target atom. In addition,

Table 2.2: Advantages and disadvantages of semiconductor doping methods [1]

Ion Implantation
+ Accurate dose and depth control
+ Applicable to most ions
+ Insensitive to dislocations and impurities
+ Several dopants may be added
+ Implantation may be at low or ambient temperature
+ Doping may be made with masks and/or a passivating layer
+ Minimal lateral spread of dopants beneath a mask
- High capital costs
- Channelling may occur and so distort the depth profile
- There is considerable radiation damage - annealing is needed
Diffusion doping
+ Relatively low cost
+ Simple equipment
- Limited choice of ions and dopant profiles
- High temperature process
- Different dopants disturb one another
- Diffusion is sensitive to dislocations and grain boundaries
- Lateral spreading of dopants beneath a mask

displaced atom may have enough kinetic energy to displace other atoms. Electronic stopping, on the hand, is loss of energy due to collisions with electrons in the target material. Electronic stopping, in general, does not cause crystal damage. Interplay between these two stopping mechanism will define the resulting ion ranges and associated damage. Light ions (or ions at higher energies) tend to loose their energy mostly due to electronic stopping whereas heavier ions (or ions at lower energy) loose their energy primarily due to nuclear stopping [1].

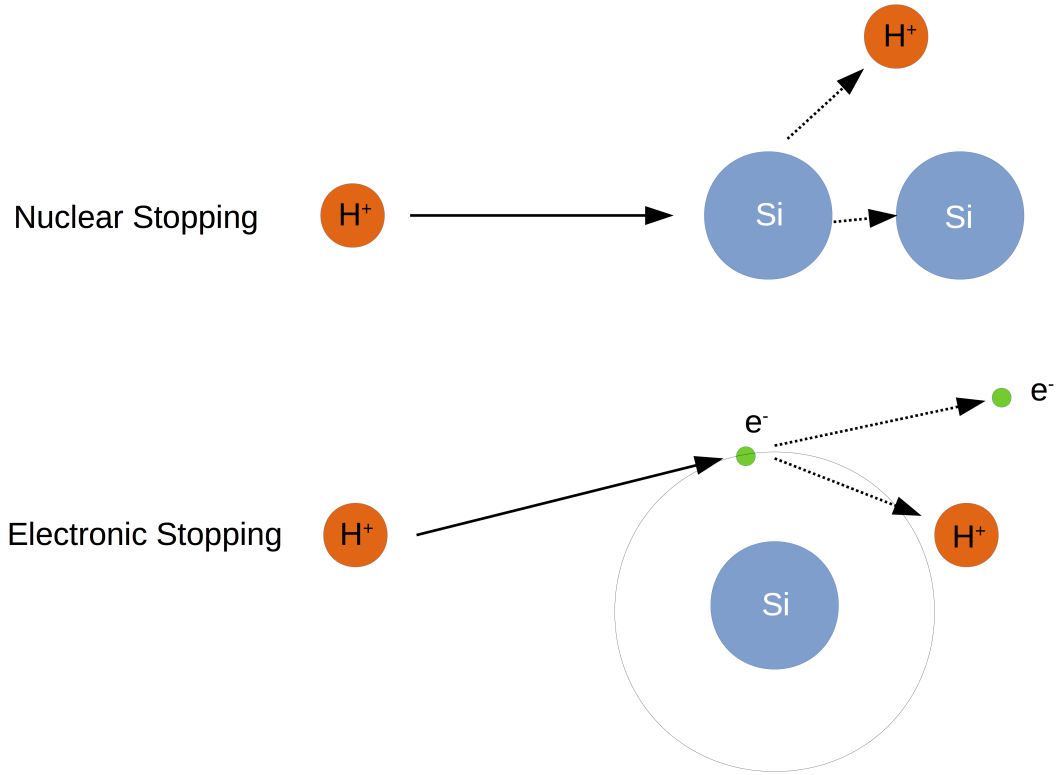

Figure 2.1: Schematic diagram of ion stopping mechanisms

The range of ions and their profile shape depends on the ion energy for a particular ion/substrate combination. The concentration of ions depends on the implantation dose. Below five profile parameters are defined for a concentration profile shown in Figure 2.2:

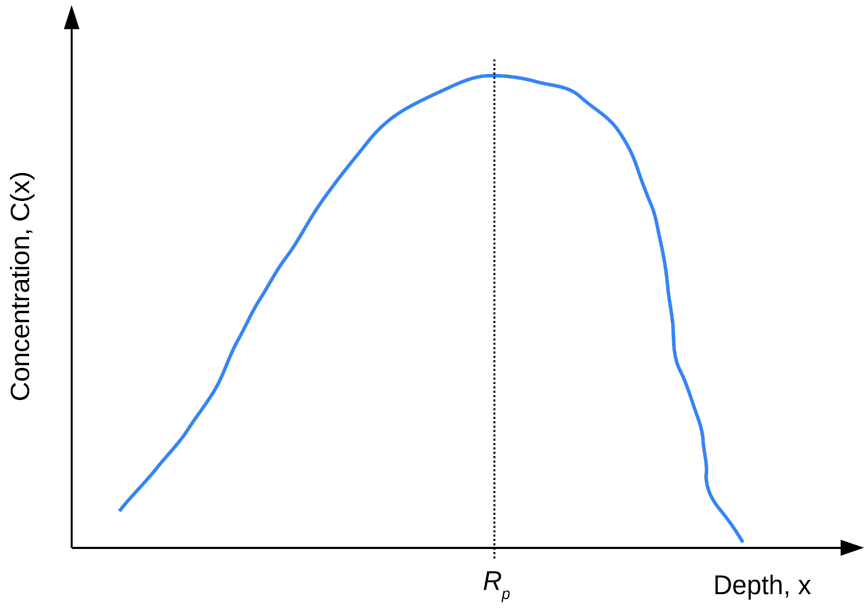

Figure 2.2: Schematic diagram of concentration profile

1. Dose of implantation: $\phi = \int_0^\infty C(x)dx$

2. Projected range: $R_p = \frac{1}{\phi}\int_0^\infty x \cdot C(x)dx$

3. Longitudinal straggle: $(\Delta R_p)^2 = \frac{1}{\phi}\int_0^\infty (x-R_p)^2 \cdot C(x)dx$

4. Skewness: $M_3 = \frac{1}{\phi}\int_0^\infty (x-R_p)^3 \cdot C(x)dx$

   Skewness describes asymmetry between left and right sides of the profile

5. Kurtosis: $M_4 = \frac{1}{\phi}\int_0^\infty (x-R_p)^4 \cdot C(x)dx$

   Kurtosis characterizes contributions of the tail regions.

The easiest way to model concentration profile of implanted species is to assume a Gaussian distribution:

$$C(x) = C_{max} \cdot e^{\frac{-(x-R_p)^2}{2(\Delta R_p)^2}}.$$

The Gaussian approximation is useful to obtain a rough estimation of profile parameters. However, actual implantation profiles are never Gaussian. Therefore, for detailed modeling of the implantation profiles more complex functions or ab-initio calculations are necessary.

One of the analytic functions that can be used instead of Gaussian is Pearson type IV distribution [38, 39, 40] that is most commonly used to date.

$$C(x) = \frac{\left|\frac{\Gamma\left(m+\frac{\nu}{2}i\right)}{\Gamma(m)}\right|^2}{\alpha \mathrm{B}\left(m-\frac{1}{2},\frac{1}{2}\right)}\left[1+\left(\frac{x-\lambda}{\alpha}\right)^2\right]^{-m}\exp\left[-\nu\arctan\left(\frac{x-\lambda}{\alpha}\right)\right], \qquad (2.1)$$

where Γ and B are gamma and beta functions, respectively. All other parameters are free variables that are used to fit a concentration profile. I will be using this function in chapter 4 to fit my experimental data. Figure 2.3 shows comparison between Pearson and Gaussian distributions.

Presently, the most used software to predict range of ions and ion implantation damage is the Stopping and Range of Ions in Matter (SRIM) code and the Transport of Ions in Matter (TRIM) code. The SRIM code calculates the stopping and range of ions up to 2 GeV/amu into matter using a quantum mechanical treatment of ion-atom collisions. The TRIM is the most comprehensive program in that it can accept complex targets made of compound materials with up to eight layers, each of a different material. It calculates the final 3D distribution of the ions and all kinetic phenomena associated with the ion's energy loss: target damage, sputtering, ionization, and phonon production [41]. Figure 2.4, as an example, shows ion ranges and quick (as opposed to detailed) damage estimation for 1.6 MeV Si implanted into SiC as calculated by the TRIM code.

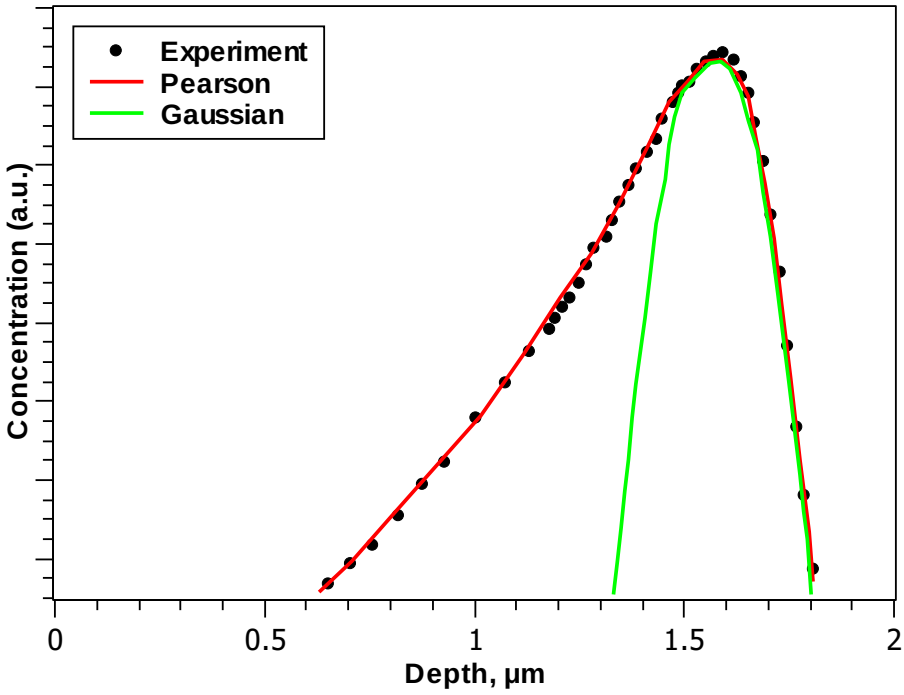

Figure 2.3: Comparison of experimental data fitting by Pearson and Gaussian distributions for 800 keV boron implanted in polycrystalline silicon. Adapted from [2]

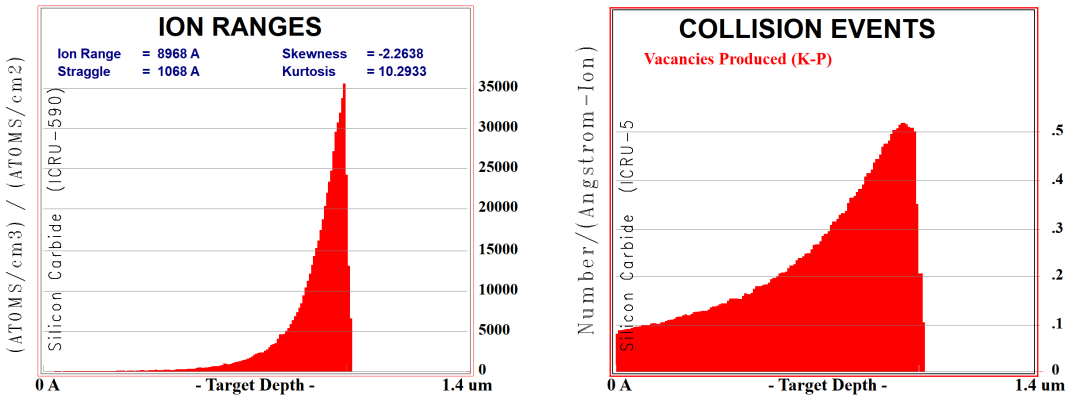

Figure 2.4: Ion ranges and quick damage estimation for 1.6 MeV Si implanted SiC

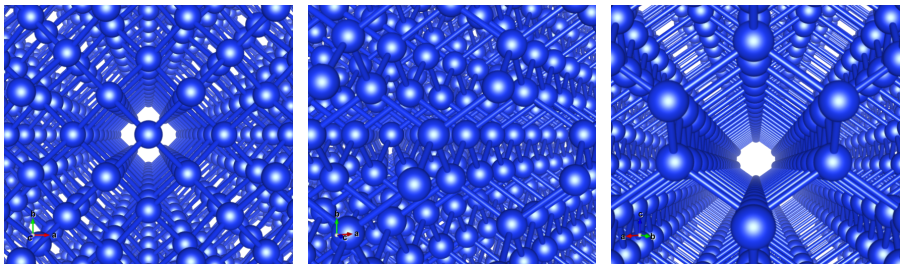

(a) Si (100) (b) 30° tilt from Si (100) (c) Si (110)

Figure 2.5: Different orientations of Si crystal generated by VESTA Software

In crystalline semiconductor substrates, particular crystallographic directions offer much lower stopping than other directions. An example of different Si crystal orientations is shown Figure 2.5. For example if an ion travels along the <110> direction in Si (see Figure 2.5c), it results in longer effective range. This effect is referred to as ion channelling. When channeling is involved it is much harder to predict ion ranges due to strong nonlinearity, i.e. small variations from perfect orientation lead to extreme differences in implantation depth. Channeling can be avoided by performing implantation through a thin amorphous layer or by tilting and twisting the sample (see Figure 2.5b, for example). For experiments discussed in this thesis, channelling was avoided by tilting the samples a few degrees off-axis.

On the other hand, Rutherford backscattering as an analytical method to determine the amount and depth profile of damage in crystalline thin film materials makes use of ion channelling.

Chapter 3

Coherent acoustic phonons

This chapter introduces the basics of picosecond laser ultrasonics that involves generation and detection of coherent acoustic phonons (CAP). This method features a nanometer spatial resolution for materials characterization in a non-destructive manner. First, we treat the generation of longitudinal acoustic waves(CAP) in semi-infinite films. Then, we consider thin ($\sim$ absorption depth of light) opaque single-layer isotropic films. Following this, we discuss detection of CAP and introduce time-domain Brillouin scattering (TDBS) which is a part of picosecond ultrasonics that focuses on analyzing Brillouin oscillations in semi-transparent and transparent materials.

Picosecond ultrasonics is a subset of the more general category of ultrafast pump-probe experiments. When an intense ultrafast ($<$1 ps) optical pump pulse is incident on a surface of opaque material, it generates a traveling CAP wave (or strain wave) due to inhomogeneous pump light absorption. The CAP wave locally alters the refractive index as it traverses the material. Thus, when an optical probe pulse is incident on a sample at a later time, its reflection and transmission is modified by the CAP wave. The interference of probe light waves reflected from the surface of the material and the traveling CAP wave results in an oscillatory time dependent reflectivity/transmissivity signal (Brillouin oscillations). Amplitude, decay and frequency of the Brillouin oscillations are highly sensitive to the optical and elastic material properties. For example, by analyzing the Brillouin oscillations, the complex refractive index (see Chapter 4) and the photoelastic coefficient (see

Chapter 5) as function of depth can be obtained.

For the efficient generation of the CAP wave, transducer layers made of metals or materials that strongly absorb at the pump energy are used [42, 43, 44, 45, 46, 47, 48, 49, 50]. The generated CAP wave travels at the longitudinal speed of sound, which leads to the obvious application of picosecond ultrasonics to thin film metrology, i.e. measuring the thicknesses of thin films by monitoring the echoes of the CAP wave [51, 52, 53]. In addition, elastic properties such as the Young modulus [54] and stress in the films [32] can be measured. Moreover, various interactions between photons, excited carriers and phonons are being studied by this technique by analyzing either the shape of the CAP pulse or the associated Brillouin oscillations. These include studies of electron diffusion [55, 56, 57, 58], shifts in the electronic energy levels by picosecond strain [59, 60, 61, 62], attenuation and dispersion of the acoustic phonons [63, 64, 42, 65, 66, 67, 68], acoustic solitons and nonlinear acoustics [69, 70, 71, 72, 73, 74], imaging biological samples [75, 76], adhesion of thin films, two dimensional materials or single cells to the substrate [77, 78, 79], out of plane energy transfer in van der Waals materials [80], ultrafast acousto-magnetoplasmonics [81, 82, 83, 84], terahertz radiation [85, 86], and specific mode acoustic phonon - electron interactions [87].

Figure 3.1 shows a schematic diagram of the generation and detection of CAP pulses. Two possible modes of the CAP wave propagation are illustrated in Figure 3.1a,b. When there is an acoustic impedance mismatch between the film and the substrate, the CAP wave gets partially reflected at the interface and returns back to the surface (Figure 3.1a). The shape of the CAP wave in this case can be measured. By studying its shape, many properties including electron diffusion and phonon attenuation, for example, can be determined.

Another case of CAP propagation is when the acoustic impedance of the film matches the acoustic impedance of the substrate, thus, allowing the CAP wave to fully transmit into the substrate. The film acts as an efficient transducer and such configuration (Figure 3.1b) allows to send CAP waves in transparent materials and study their properties. Such configuration is used in experiments outlined in this thesis.

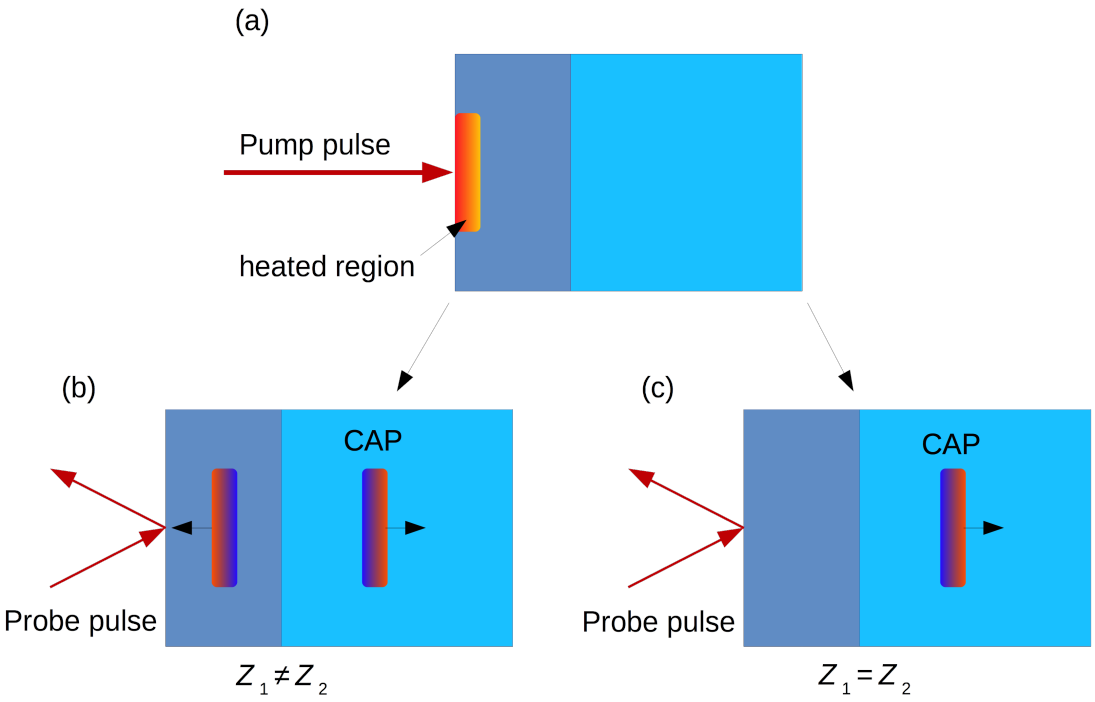

Figure 3.1: Schematic diagram of picosecond ultrasonics experiment. a) Ultrafast optical pump pulse heats up the surface of the film and generates acoustic pulse, b) in case of acoustic impedance (Z) mismatch between the film and the substrate, the acoustic wave both reflected back and transmitted into the substrate c) Acoustic wave is transmitted into the substrate because of perfect acoustic impedance matching.

3.1 Generation of coherent acoustic phonons

3.1.1 CAP generation in semi-infinite layer

In this thesis, only metals were be used as a transducer layer to generate coherent acoustic phonons. Therefore, coherent acoustic phonon generation only by thermal stress will be reviewed. Derivation follows Matsuda et. al. [88].

When an ultrafast optical pulse (<1ps) is absorbed by a material, it induces a thermal stress. Below are some assumptions that are routinely taken into account to derive an analytic expression for the propagating strain pulse (CAP wave):

1. infinitely short optical pulse
2. semi-infinite solid
3. illumination area is orders of magnitude larger than the optical absorption depth, so that the problem becomes one-dimensional
4. no electron and thermal diffusion

The stress-strain relation in the presence of thermal stress is written as:

$$\sigma_{ij} = c_{ijkl}\eta_{kl} + \sigma'_{ij}, \tag{3.1}$$

where σ_{ij} is the stress tensor, c_{ijkl} is the elastic constant tensor, η_{kl} is strain, and σ'_{ij} is the termal stress tensor. At times $t = \infty$, $\sigma_{ij} = 0$ and $\eta_{ij} = \alpha_{ij}\Delta T$, where α_{ij} is the thermal expansion tensor and ΔT is the temperature change due to optical pulse.

From equation 3.1, it follows that $\sigma'_{ij} = -c_{ijkl}\alpha_{kl}\Delta T$. For isotropic solids, this results in

$$\sigma'_{ij} = -3B\alpha\delta_{ij}\Delta T, \tag{3.2}$$

where B is the bulk modulus, α is the linear thermal expansion coefficient. For positive α and ΔT, the generated thermal stress is hydrostatic and compressive.

For one dimension, we rewrite the stress-strain relation 3.1 as

$$\sigma_{zz} = \rho_0 v_l^2 \eta_{zz} - 3B\alpha\Delta T(z), \tag{3.3}$$

where ρ_0 is the density and v_l is the longitudinal sound velocity.

The change in temperature due absorbed optical pulse is

$$\Delta T(z) = \frac{(1-R)Q}{AC\zeta_0} e^{-\frac{z}{\zeta_0}}, \text{for } t > 0, \quad \Delta T(z) = 0, \text{for } t < 0, \tag{3.4}$$

where R is the optical reflection coefficient, Q is the optical pulse energy, A is the illuminated area, C is the heat capacity per unit volume, and ζ_0 is the optical absorption depth of the pump light.

The elastic wave equation is given by

$$\frac{\partial \sigma_{zz}}{\partial z} = \rho_0 \frac{\partial^2 u_z}{\partial t^2}, \tag{3.5}$$

where $\eta_{zz} = \partial u_z / \partial z$.

From the boundary condition at the free surface, $\sigma_{zz} = 0$ at $z = 0$ and equation 3.1, we

get

$$\eta_{zz}(z=0,t)=\eta_0=\frac{3B\alpha(1-R)Q}{AC\zeta_0\rho_0 v_l^2} \tag{3.6}$$

The equation 3.5 can be written in terms of displacement u_z as

$$\frac{\partial^2 u_z}{\partial t^2}=v_l^2\frac{\partial^2 u_z}{\partial z^2}+\frac{v_l^2\eta_0}{\zeta_0}e^{-\frac{z}{\zeta_0}} \tag{3.7}$$

The elastic wave equation 3.5 can be solved analytically with initial conditions, $\eta_{zz}=0$, $\partial\eta_{zz}/\partial t=0$, and $u_z=0$ for all z for $t<0$ [88]:

$$\eta_{zz}=\eta_0 e^{-\frac{z}{\zeta_0}}-\frac{\eta_0}{2}\left[e^{-\frac{z+v_l t}{\zeta_0}}+e^{-\frac{|z-v_l t|}{\zeta_0}}sgn(z-v_l t)\right] \tag{3.8}$$

The equation 3.8 is plotted in Figure 3.2. The strain consist of two terms: constant and propagating. They both are depicted in Figure 3.2. Bipolar shape of the strain is due to reflection at the free surface. The wavelength of this strain wave and the frequency of the maximum strain amplitude is $2\pi\zeta_0$ and $f=v_l/(2\pi\zeta_0)$, respectively.

When one includes in the calculation diffusion processes, the generated strain pulse is broadened [55, 57, 88]. In general, there are several strain generation mechanisms that must be taken into account if non-metals are used to photo-generate strain waves[89]. In this thesis, metals were used to generate strain waves, thus only the thermoelastic mechanism is considered.

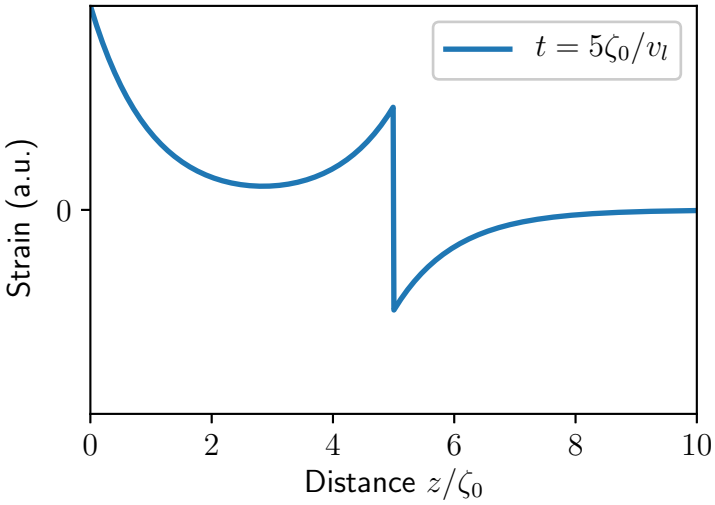

Figure 3.2: Strain for $\zeta_0 = 8$ nm and $v_l = 6.42$ nm/ps

3.1.2 CAP generation in thin films on a substrate

In a previous section, the generation of acoustic pulses in a semi-infinite film was discussed. When electron/thermal diffusion and finite thickness of the film are taken into account, the solution 3.8 can be approximated by derivative of a Gaussian function [59]:

$$\eta(t) = \frac{2A\xi}{v_l\tau^2}(1-r)\sum_{j=0}^{\infty} r^j \left(t - \frac{(2j+1)d}{v_l}\right) \exp\left[-\frac{1}{\tau^2}\left(t - \frac{(2j+1)d}{v_l}\right)^2\right], \tag{3.9}$$

where ξ is the absorption depth of the pump light, r is the reflection coefficient of longitudinal acoustic waves at the interface between film and substrate, d is the thickness of the film, and v_l is the sound velocity in the film. A is a dimensionless coefficient which depends on pump intensity and the film parameters:

$$A = \frac{3(1-R)W\beta B}{2C\xi\rho v_l^2}, \tag{3.10}$$

where R is the pump light reflection coefficient, W is the pump fluence (J/m^2), β is the linear expansion coefficient, B is the bulk modulus, C is the volumetric heat capacity, and ρ is the film density. $\tau \geq \xi/v_l$ is an adjustable parameter defining the width of the pulse. It is governed by electron diffusion [45, 90] and imperfections in the metal film.

Assuming perfect acoustic impedance between the film and the substrate, and ideal situation when $\tau = \xi/v_l$, we can rewrite equation 3.9 in another form:

$$\eta(z,t) = -\eta_0 \frac{(z - v_l t)}{\xi} \exp\left[-\frac{(z - v_l t)^2}{\xi^2}\right], \tag{3.11}$$

where

$$\eta_0 = 2A(1 - r). \tag{3.12}$$

The shape of the pulse according to the equation 3.11 is plotted in Figure 3.3. Compared to Figure 3.2, the strain wave is broadened accounting for diffusion effects during strain generation.

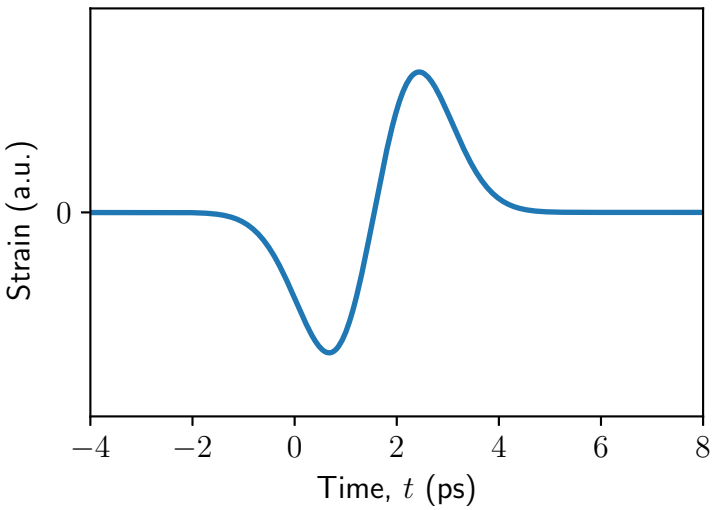

Figure 3.3: Strain pulse plotted from equation 3.11

3.2 Detection of coherent acoustic phonons

When the strain wave travels through a crystal it perturbs its dielectric constant, $\varepsilon = (n+i\kappa)^2$. The perturbation of the dielectric constant due to strain can be written as:

$$\Delta\varepsilon(z,t) = \Delta(\tilde{n})^2 \cong 2\tilde{n}\Delta\tilde{n} = 2(n+i\kappa)\left(\frac{\partial n}{\partial \eta} + i\frac{\partial \kappa}{\partial \eta}\right)\eta(z,t) \tag{3.13}$$

where the quantities $\partial n/\partial\eta$ and $\partial\kappa/\partial et\ al.$ are related to the photoelastic coefficients P_{12} as follows [91]:

$$P_{12} = \frac{\partial \varepsilon_{xx}}{\partial \eta} = 2\tilde{n}\left(\frac{\partial n}{\partial \eta} + i\frac{\partial \kappa}{\partial \eta}\right). \tag{3.14}$$

In general, photoelastic coefficients are wavelength dependent. The equation 3.14 is valid for isotropic materials.

By solving Maxwell equations with a perturbed dielectric constant (Equation 3.13), it can be shown that the relative change in reflectance from a material perturbed by propagating strain wave is [88].

$$\frac{\delta r(t)}{r_0} = \frac{2ik}{1-\varepsilon}\int_0^\infty \Delta\varepsilon(z',t)e^{2ik_1 z'}dz' = \frac{4ik\tilde{n}}{1-\tilde{n}^2}\frac{d\tilde{n}}{d\eta}\int_0^\infty \eta(z',t)e^{2ik\tilde{n}z'}dz' \tag{3.15}$$

The reflectance $\delta r/r_0$ is related to measured reflectivity $\Delta R/R_0$ as follows:

$$\frac{\delta R}{R_0} = 2\mathrm{Re}\left(\frac{\delta r}{r_0}\right) \tag{3.16}$$

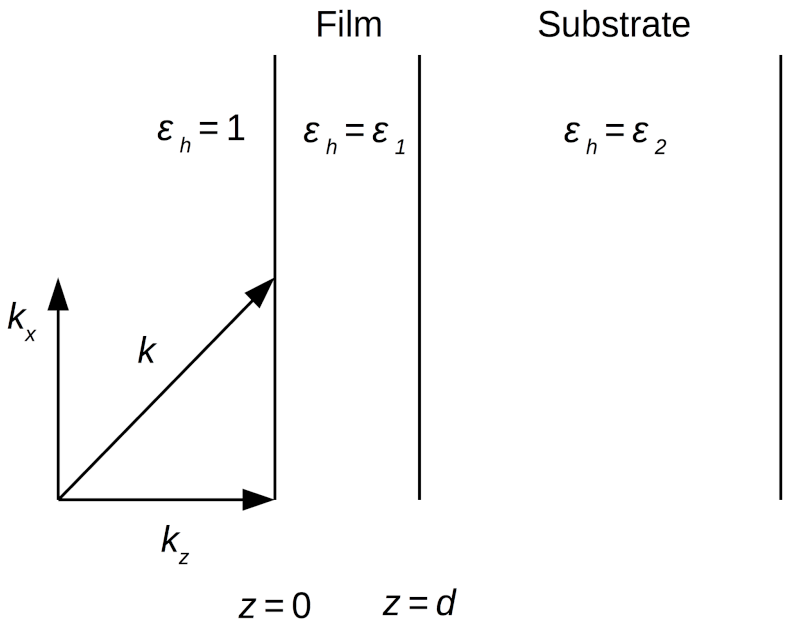

Figure 3.4: Geometrical configuration of the system. Light is incident from $z < 0$. Wavevector k_x is the same for incident, reflected and transmitted light rays.

3.2.1 Reflectivity in two-layer system

Consider a sample consisting of a thin layer and a substrate. The configuration of the system is shown in figure 3.4. Each layer is assumed to be homogeneous and isotropic so that the permittivity tensor, $\varepsilon_h(z)$ can be considered staircase-like function. While the acoustic pulse propagates, it modulates the permittivity tensor via the photoelastic effect and temporarily creates surface and interface displacements. Let us define change in the permittivity due to the strain pulse as $\varepsilon_{ih}(z,t)$.

In order to calculate the change in the complex optical reflectance, the electromagnetic wave equation 3.17 with an inhomogeneously perturbed permittivity tensor $\varepsilon_h(z) + \varepsilon_{ih}(z,t)$

can be solved [92].

$$\left[L(k_x)+k^2\{\varepsilon_h(z)+\varepsilon_{ih}(z,t)\}\right]E(z,t)=0, \tag{3.17}$$

where $k=\omega/c$ is the wave vector in vacuum and the operator matrix $L(k_x)$ is given by

$$L(k_x)=\begin{pmatrix} \frac{\partial^2}{\partial z^2} & 0 & -ik_x\frac{\partial}{\partial z} \\ 0 & \frac{\partial^2}{\partial z^2}-k_x^2 & 0 \\ -ik_x\frac{\partial}{\partial z} & 0 & -k_x^2 \end{pmatrix}.$$

The perturbation in the permittivity $\varepsilon_{pe}(z,t)$ due to acoustic wave in an isotropic material depends on the strain $\eta_{zz}(z,t)$ and photoelastic tensor components P_{11} and P_{12} as

$$\varepsilon_{pe}(z,t)=\begin{pmatrix} P_{12}^{(j)} & 0 & 0 \\ 0 & P_{12}^{(j)} & 0 \\ 0 & 0 & P_{11}^{(j)} \end{pmatrix}\eta_{zz}(z,t), \tag{3.18}$$

where index j indicates layer number. The complex reflectance change for s- and p-polarized light is then given by [92]:

$$\begin{aligned}\frac{\delta r^{(s)}}{r^{(s)}}=\frac{ik^2}{2k_0a_0^{(s)}b_0^{(s)}}\Bigg[&P_{12}^{(1)}\int_0^d\eta(z',t)\left(a_1^{(s)}e^{ik_1z'}+b_1^{(s)}e^{-ik_1z'}\right)^2dz' \\ &+P_{12}^{(2)}\int_0^{\infty}\eta(z'+d,t)\left(a_2^{(s)}e^{ik_2z'}\right)^2dz' \\ &+u(0,t)(1-\varepsilon_1)\left(a_1^{(s)}+b_1^{(s)}\right)^2+u(d,t)(\varepsilon_1-\varepsilon_2)\left(a_2^{(s)}\right)^2\Bigg],\end{aligned} \tag{3.19}$$

$$\frac{\delta r^{(p)}}{r^{(p)}} = \frac{i}{2k_0 a_0^{(p)} b_0^{(p)}} \left[\frac{k_1^2}{\varepsilon_1} P_{12}^{(1)} \int_0^d \eta(z',t) \left(a_1^{(s)} e^{ik_1 z'} + b_1^{(s)} e^{-ik_1 z'} \right)^2 dz' \right.$$

$$+ \frac{k_x^2}{\varepsilon_1} P_{11}^{(1)} \int_0^d \eta(z',t) \left(a_1^{(s)} e^{ik_1 z'} - b_1^{(s)} e^{-ik_1 z'} \right)^2 dz'$$

$$+ \frac{k_2^2 P_{12}^{(2)} - k_x^2 P_{11}^{(2)}}{\varepsilon_2} \int_0^\infty \eta(z'+d,t) \left(a_2^{(p)} e^{ik_2 z'} \right)^2 dz' \tag{3.20}$$

$$+ u(0,t)(1-\varepsilon_1) \left\{ \frac{k_1^2}{\varepsilon_1} \left(a_1^{(p)} + b_1^{(p)} \right)^2 - k_x^2 \left(a_1^{(p)} - b_1^{(p)} \right)^2 \right\}$$

$$\left. + u(d,t)(\varepsilon_1 - \varepsilon_2) \left(\frac{k_2^2}{\varepsilon_2} - \frac{k_x^2}{\varepsilon_1} \right) \left(a_2^{(s)} \right)^2 \right],$$

where $r^{(\mu)} = b_{(0)}^{(\mu)} / a_{(0)}^{(\mu)}$ is the reflectance for the unperturbed (by the strain wave) sample, d is the thickness of the transducer layer, $k_j = \sqrt{\varepsilon_j k^2 - k_x^2}$ is the wave vector in j-th medium, k is the wave vector in vacuum, a_j and b_j are the electric field amplitudes in j-th layer, u is the displacement, and ε_1 and ε_2 are the dielectric constants of the transducer and the

substrate, respectively. The electric field amplitudes are given by [92]:

$$
\begin{aligned}
a_0^{(s)} &= (k_0-k_1)(k_1-k_2)e^{2ik_1d}+(k_0+k_1)(k_1+k_2),\\
b_0^{(s)} &= (k_0+k_1)(k_1-k_2)e^{2ik_1d}+(k_0-k_1)(k_1+k_2),\\
a_1^{(s)} &= 2k_0(k_1+k_2),\\
b_1^{(s)} &= 2k_0(k_1-k_2)e^{2ik_1d},\\
a_2^{(s)} &= 4k_0k_1e^{ik_1d},\\
a_0^{(p)} &= (\varepsilon_1k_0-k_1)(\varepsilon_2k_1-\varepsilon_1k_2)e^{2ik_1d}+(\varepsilon_1k_0+k_1)(\varepsilon_2k_1+\varepsilon_1k_2),\\
b_0^{(p)} &= -(\varepsilon_1k_0+k_1)(\varepsilon_2k_1-\varepsilon_1k_2)e^{2ik_1d}-(\varepsilon_1k_0-k_1)(\varepsilon_2k_1+\varepsilon_1k_2),\\
a_1^{(p)} &= 2\sqrt{\varepsilon_1}k_0(\varepsilon_2k_1+\varepsilon_1k_2),\\
b_1^{(p)} &= -2\sqrt{\varepsilon_1}k_0(\varepsilon_2k_1-\varepsilon_1k_2)e^{2ik_1d},\\
a_2^{(p)} &= 4\varepsilon_1\sqrt{\varepsilon_2}k_0k_1e^{ik_1d}.
\end{aligned}
\tag{3.21}
$$

3.3 Energy dependence of the acoustic deformation potential in GaP

In this section, we will discuss the energy dependence of the amplitude of the Brillouin oscillations as measured in experiments and how it can be used to determine the energy dependence of the acoustic deformation potential. Experimental results will be given for gallium phosphide.

In general, when one models the time-dependent Brillouin scattering optical response, knowledge of the acoustic deformation potential or photoelastic coefficients is necessary. In particular, certain issues arise for indirect band gap semiconductors in an energy range close to their indirect and direct band gaps. In this energy range, multiple optical transitions must be taken into account, which leads to significant dependence of the deformation potential on energy. In a recent paper, Ishioka et al. showed that there is a discrepancy between experimental and theoretical amplitudes of the Brillouin oscillations in GaP for probe energies below its direct band gap when the energy dependence of the deformation potential is neglected [4]. This discrepancy between modelling and experiment suggests a way to measure the energy dependence of the deformation potential in semiconductors in an energy range that is not available by other methods.

Originally, deformation potential theory was developed by Bardeen and Shockley. The deformation potential describes the strength of electron – acoustic phonon scattering [93]. When a solid is subject to a strain, $s_{\alpha\beta}$, there will be a change in band energy levels:

$$\delta E_n(\vec{k}) = \sum_{\alpha\beta} \Xi_{\alpha\beta}(n,\vec{k}) s_{\alpha\beta}, \tag{3.22}$$

where $\Xi_{\alpha\beta}(n,\vec{k})$ is the deformation potential, and the indices $\alpha\beta$ describe strain tensor, $s_{\alpha\beta}$, components. Here, we are only concerned with uniaxial strain and the deformation potential between the valence and conduction bands that is denoted as a_{cv}.

3.3.1 Derivation of amplitude of Brillouin oscillations

The amplitude of Brillouin oscillations can be derived for a two layer system where the first layer acts as a transducer layer to generate acoustic pulses. The second layer is a substrate and is the layer wherein we want to find the amplitude of Brillouin oscillations as the acoustic pulse traverses it.

The first term in equation 3.19 and first two terms in equation 3.20 describe contributions to the reflectivity change when the strain wave is traveling through the transducer layer. Once it leaves the layer, these terms vanish. We ignore any contribution from the static strain caused by the elevated temperature of the transducer layer. Terms that include displacement of the surface and the interface, $u(z,t) = \int_{-\infty}^{z} \eta(z',t)dz'$, also vanish when the strain wave is transmitted into the substrate. Therefore, we can rewrite equations 3.19 and 3.20 as follows

$$\frac{\delta r^{(s)}}{r^{(s)}} = \frac{ik^2}{2k_0 a_0^{(s)} b_0^{(s)}} P_{12}^{(2)} \int_0^{\infty} \eta(z'+d,t)\left(a_2^{(s)} e^{ik_2 z'}\right)^2 dz', \tag{3.23}$$

$$\frac{\delta r^{(p)}}{r^{(p)}} = \frac{i}{2k_0 a_0^{(p)} b_0^{(p)}} \frac{k_2^2 P_{12}^{(2)} - k_x^2 P_{11}^{(2)}}{\varepsilon_2} \int_0^{\infty} \eta(z'+d,t)\left(a_2^{(p)} e^{ik_2 z'}\right)^2 dz'. \tag{3.24}$$

For simplicity, I will omit label (2) in $P_{ij}^{(2)}$ because we will be only concerned about the

substrate. The photoelastic coefficient is by definition [91]

$$P_{12} = \frac{\partial \varepsilon}{\partial \eta}. \tag{3.25}$$

We can approximate that the strain modulates the permittivity by changing the band gap of a semiconductor by deformation potential [4, 94, 95],

$$\varepsilon(E, \eta) \backsimeq \varepsilon(E - a_{cv}\eta). \tag{3.26}$$

The strain amplitude used in picosecond ultrasonics experiments is of the order of 10^{-5} and the deformation potential for a common semiconductor is about 10 eV. Therefore, the term $a_{cv}\eta$ is much smaller than E. Taking this into account, the equation 3.25 can be written as

$$P_{12} = \frac{\partial \varepsilon}{\partial \eta} \backsimeq -a_{cv}(E)\frac{\partial \varepsilon}{\partial E}. \tag{3.27}$$

In general, the deformation potential, $a_{cv}(E)$, is a function of energy. Let us plug equation 3.27 into equation 3.28 to determine the probe energy dependence of the Brillouin oscillation amplitude

$$\frac{\delta r^{(s)}}{r^{(s)}} = \frac{ik^2}{2k_0 a_0^{(s)} b_0^{(s)}} \left(-a_{cv}\frac{\partial \varepsilon}{\partial E}\right) \int_0^\infty \eta(z' + d, t)\left(a_2^{(s)} e^{ik_2 z'}\right)^2 dz'. \tag{3.28}$$

If we assume that the generated pulse is described by equation 3.11, then the integral in

equation 3.28 becomes

$$\int_0^\infty (z-vt+d)e^{-\frac{(z-vt+d)^2}{\xi^2}} e^{2ik_2 z}dz = \\ = \frac{\xi^2}{2}e^{-\frac{(d-vt)^2}{\xi^2}}\left(1-i\sqrt{\pi}k_2\xi e^{\frac{\left(d-vt+i\xi^2k_2\right)^2}{\xi^2}}\text{Erfc}\left[\frac{d-vt}{\xi}+i\xi k_2\right]\right). \tag{3.29}$$

The complex reflectance from equation 3.28 becomes

$$\frac{\delta r}{r_0} = C_4 e^{-\frac{(d-vt)^2}{\xi^2}} - iC_4\sqrt{\pi}\xi k_2 \text{Erfc}\left[\frac{d-vt}{\xi}+i\xi k_2\right] e^{-\xi^2k_2^2}e^{2ik_2(d-vt)}. \tag{3.30}$$

Only the second term in equation 3.30 results in Brillouin oscillations. The complementary error function, Erfc $\left[\frac{d-vt}{\xi}+i\xi k_2\right]$ is essentially 2 at longer times. Therefore, the amplitude of the Brillouin oscillations may be expressed as:

$$A_{osc} = \left|-4iC_4\sqrt{\pi}\xi k_2 e^{-\xi^2k_2^2}\right|, \tag{3.31}$$

where

$$C_4 = \eta_0\frac{ik^2}{2k_0a_0b_0}a_2^2\left(a_{cv}\frac{\partial\varepsilon}{\partial E}\right)\frac{\xi}{2}. \tag{3.32}$$

Finally, the resulting amplitude of the Brillouin oscillations can be expressed as

$$A_{osc} = \sqrt{\pi}\eta_0\xi^2 a_{cv}(E)\left|\frac{k^2k_2a_2^2}{k_0a_0b_0}\frac{\partial\varepsilon}{\partial E}\right|_{E=\hbar ck} e^{-\xi^2k_2^2}\Bigg|. \tag{3.33}$$

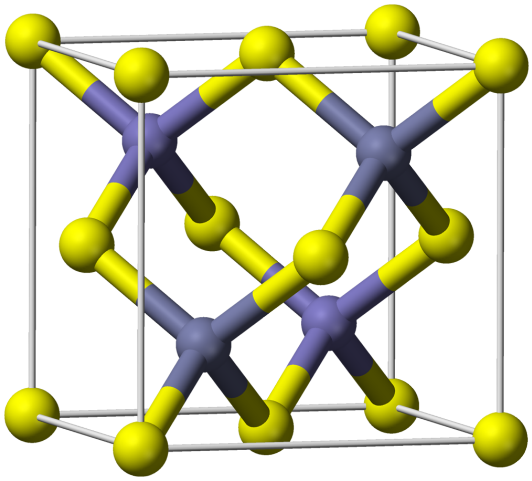

Figure 3.5: Zinc Blende crystal structure

3.3.2 Deformation potential of gallium phosphide

Gallium phosphide (GaP) is a compound semiconductor with an indirect band gap of 2.26 eV [96]. It has a zinc blende crystal structure (see Figure 3.5). GaP is and ideal candidate for photonic structures in the visible range due to its high refractive index and low absorption coefficient [3]. Most commonly it is used in manufacturing low-cost red, orange, and green light-emitting diodes (LEDs) with low to medium brightness.

Recently, the generation of broadband THz pulses by optical rectification in GaP waveguides [97, 98, 99, 100, 101] was demonstrated. The dispersion of the GaP emitter and the peak frequency of the emitted THz radiation are tunable. Also, the use of a waveguide for the THz emission offers scalability to higher power and represents the highest average power for a broadband THz source pumped by fiber lasers [97].

In order to perform time-domain Brillouin scattering experiments, a 20 nm titanium layer was deposited using an Angstrom e-beam evaporator with a 2 Å/s deposition rate

to serve as a transducer for the CAP wave. Ti was chosen as it has an excellent acoustic impedance matching with GaP (10%) which suppresses acoustic reflection at their interface.

Time-domain Brillouin scattering measurements were performed in a standard time-resolved pump-probe setup in reflection geometry. A Coherent Mira 900 with 150-fs pulses at 76 MHz was used as a laser source. Wavelength of the laser was varied. Probe power (10 mW at 800 nm) was significantly smaller than the pump power (200 mW at 800 nm). In order to generate probe wavelength in the UV range, BBO crystal was used. BBO crystal is a nonlinear material that can generate light at twice frequency of the incoming light due to high nonlinear susceptibility. The angle of incidence of the probe beam was 30°. Both beams were focused onto the specimen with spot diameters of 100 μm and 90 μm for pump and probe, respectively. The pump beam was chopped using a Thorlabs optical chopper operating at about 3 kHz. For energies out of the range of the Coherent Mira 900 (750 nm - 900 nm, 375 nm - 450 nm), the Spectra Physics Spitfire Ace amplifier system was used. The pump wavelength was set to 800 nm. For the probe beam, white light generated in a sapphire crystal was used. The probe wavelength was selected using a narrow band pass filter. The repetition rate of the amplifier system was set to 1 kHz. The pump beam was chopped at 0.5 kHz.

Figure 3.6 shows time domain Brillouin oscillations in GaP for selected different wavelengths. Thermal background arising from hot electrons in the Ti layer was subtracted from the data. It can be seen that the amplitude of the Brillouin oscillations varies with probe wavelength. The amplitude of the Brillouin oscillations was extracted from the data by fitting it with a decaying sine wave.

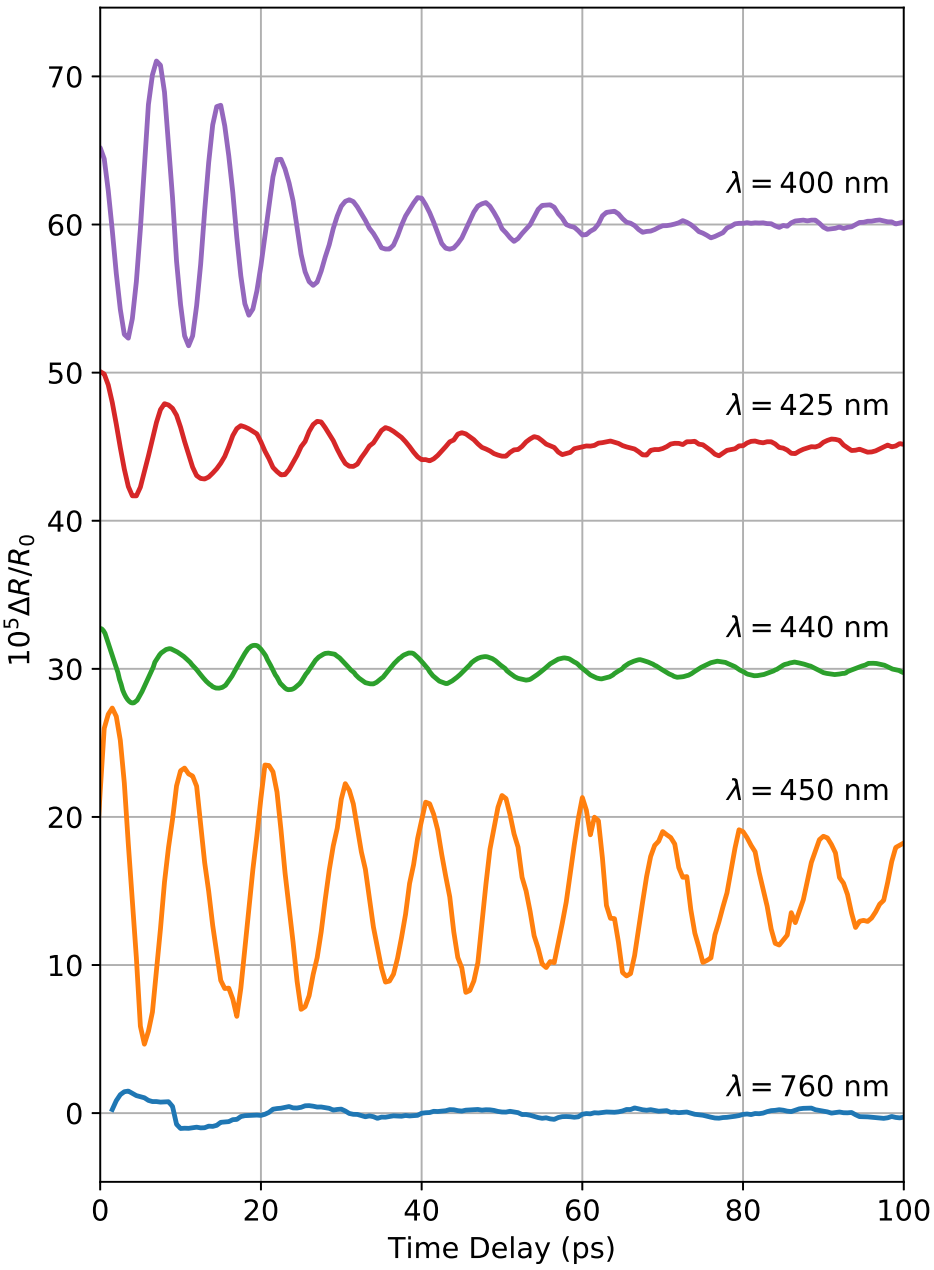

Figure 3.6: Time domain Brillouin oscillations in GaP for different wavelengths.

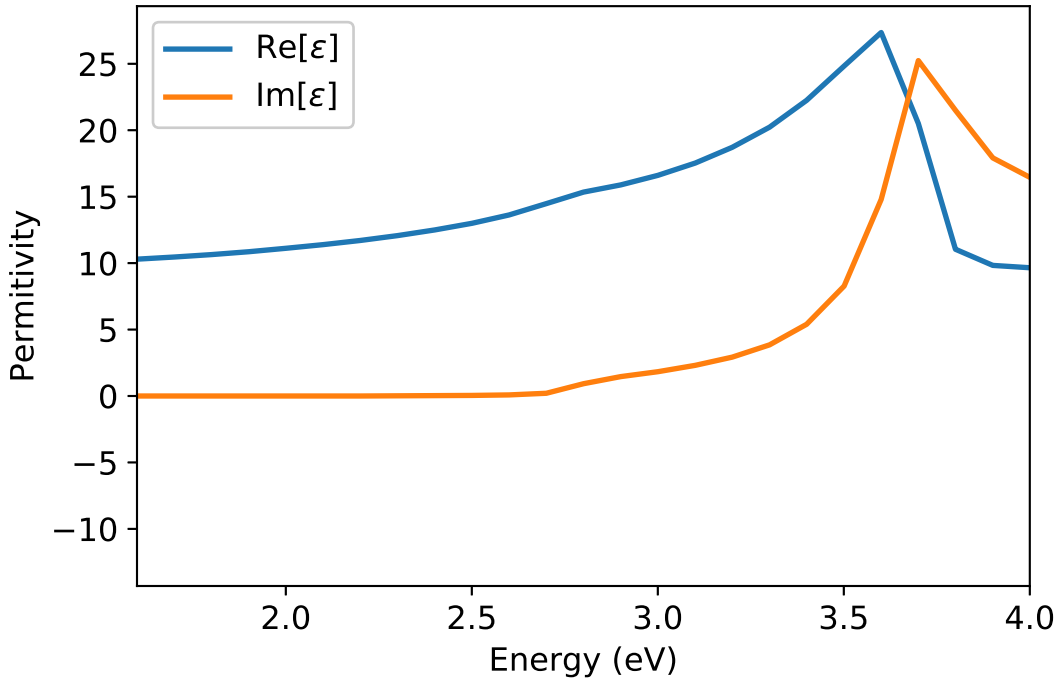

Figure 3.7: Real and imaginary parts of the permittivity of GaP [3]

Equation 3.33 includes the derivative of the permittivity. Figure 3.7 shows the dependence of the permittivity of GaP with respect to energy. Next, we take the energy derivative of the permittivity. The results are shown in Figure 3.8. One can observe two resonant transitions. The one around 2.78 eV [102] corresponds to the direct band gap of GaP.

The experimental amplitude of the Brillouin oscillations and the amplitude modeled by the equation 3.33 is presented in Figure 3.9 and 3.10. Additional experimental data are also taken from previous studies [4]. The deformation potential is taken from the literature $a_{cv} = -3.07$ [103]. Table 3.1 lists the parameters used for simulation of the amplitude of the Brillouin oscillations.

There is significant discrepancy between the model and the experiment, when the deformation potential is assumed to be constant with respect to energy. Therefore, it suggests

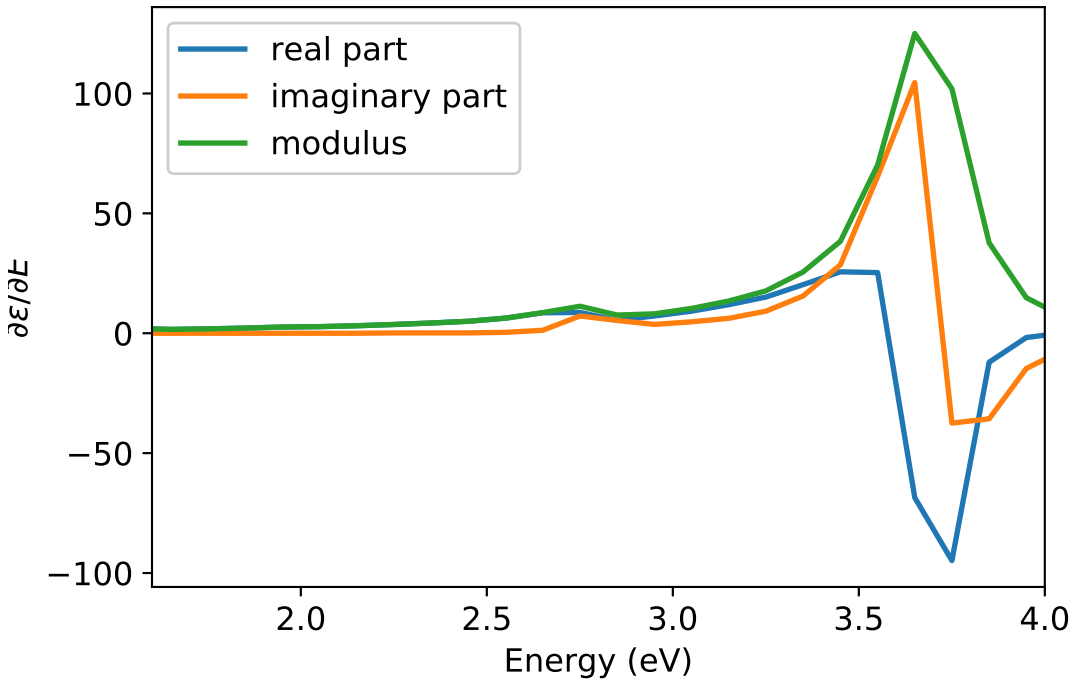

Figure 3.8: The energy derivative of the permittivity

Table 3.1: Parameters for Ti used in the model to calculate strain amplitude, η_0

Physical quantity	Value
Absorption depth at 800 nm, ξ	19.37 nm
Linear expansion coefficient, β	8.6×10^{-6} K^{-1}
Bulk modulus, B	110 GPa
Volumetric heat capacity, c	2.453×10^{-6} J/(m^{3}K)
Density, ρ	4506 kg/m^3
Sound velocity, v_l	6100 m/s
Reflection coefficient at 800 nm, R	0.5178

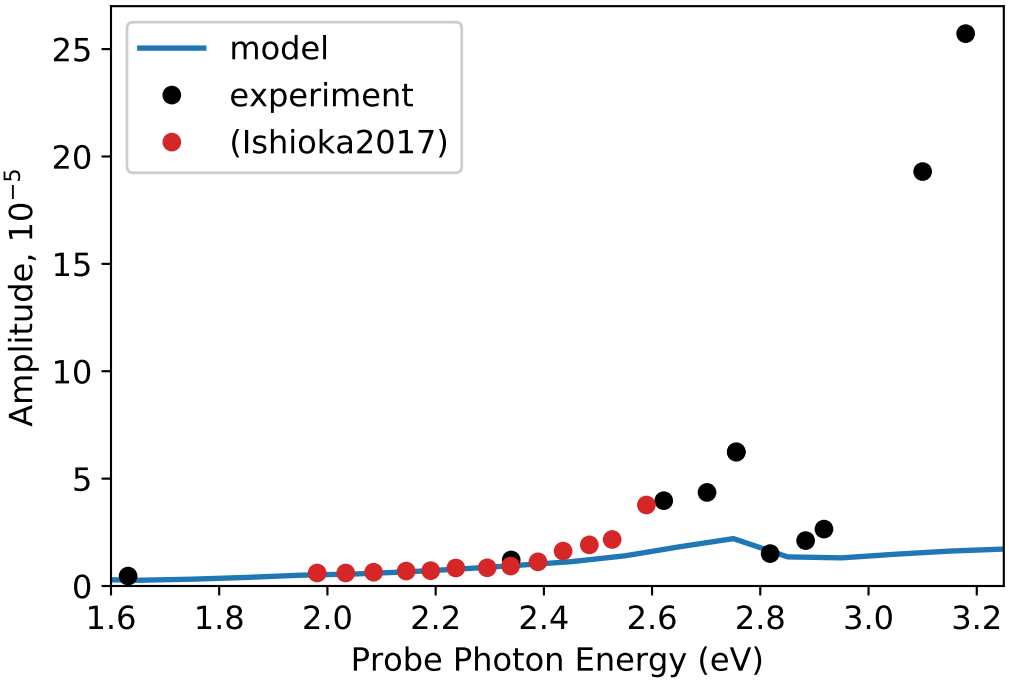

Figure 3.9: Experimental amplitude of Brillouin oscillations in GaP (black dots and red dots [4]) and predicted amplitude with $a_{cv} = -3.07$

a way to determine the dependence of the deformation potential on energy. That is we are going to divide our experimental data by the model which will leave us with energy dependent function that is normalized on the $a_{cv} = -3.07$.

Figures 3.11 and 3.12 show the energy dependence of the acoustic deformation potential as obtained from the comparison between the model and the experimental data. Our results show that the acoustic deformation potential is strongly dependent on energy above the indirect band gap of GaP (2.26 eV [96]). The first peak is observed to be near the direct optical transition at the Γ point, 2.78 eV [102], then it drops and increases further towards another direct optical transition near the L point (zone boundary), ~ 3.55 eV [104], which is out of range in the current study. Thus, the dependence of the acoustic deformation po-

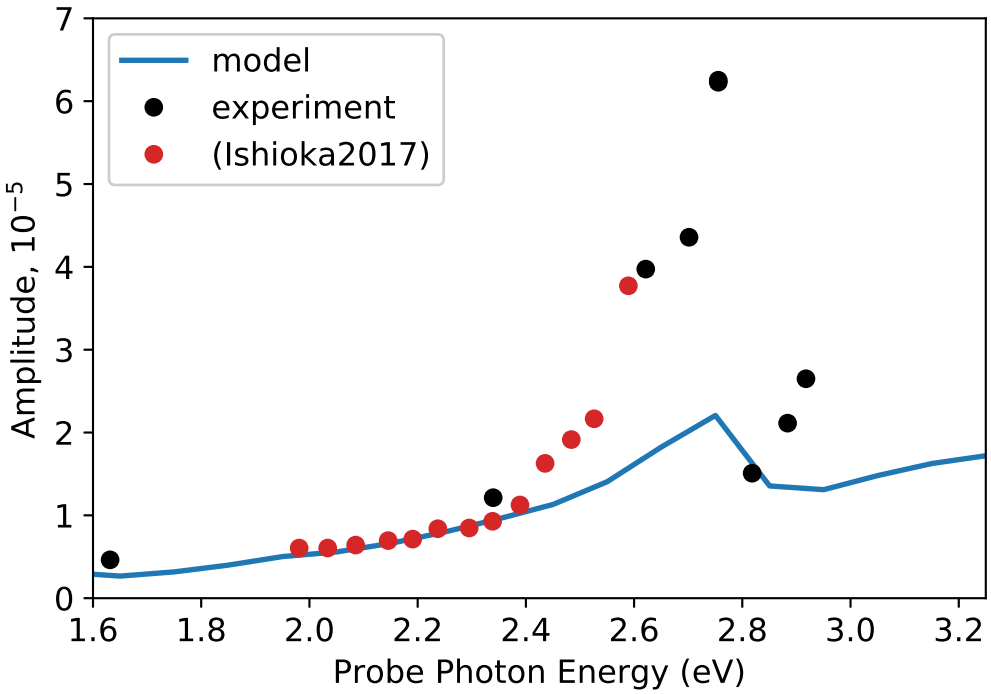

Figure 3.10: Experimental amplitude of Brillouin oscillations in GaP (black dots and red dots [4]) and predicted amplitude with $a_{cv} = -3.07$

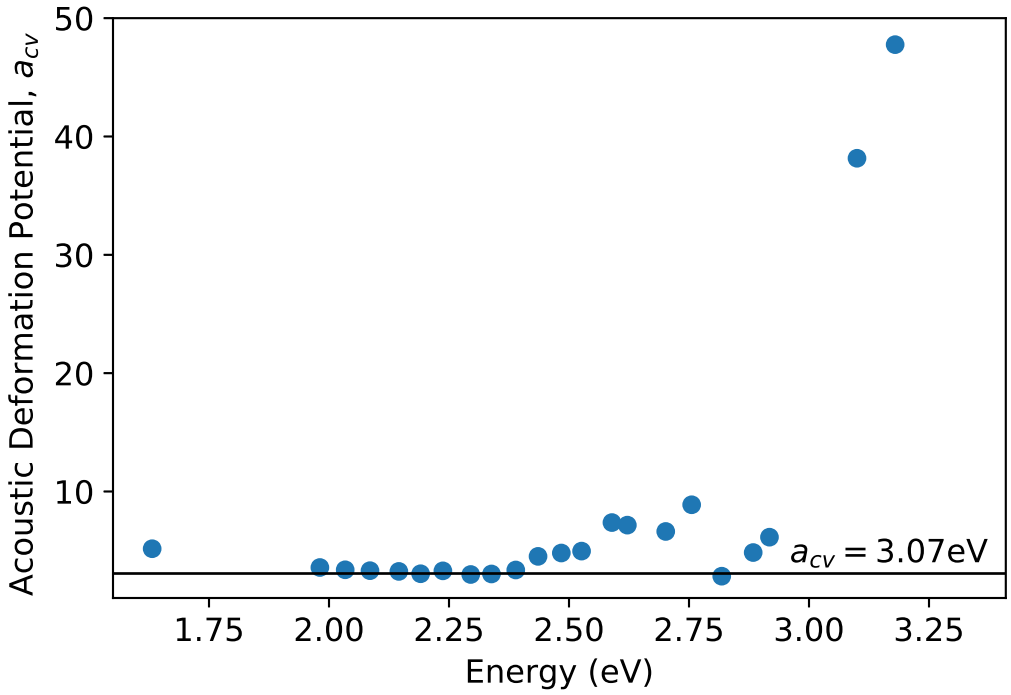

Figure 3.11: Magnitude of the acoustic deformation potential as a function of energy, $|a_{cv}| = 3.07$.

tential on energy can be explained by multiple optical transitions contributing above the indirect band gap.

In conclusion, we have shown in this section how the acoustic deformation potential can be measured using time-domain Brillouin scattering. Our results indicate strong energy dependence of the deformation potential above the indirect band gap of gallium phosphide. The deformation potential reaches peak at the Γ point and increases towards the L point. Similar behaviour in the amplitude of the Brillouin oscillations have been observed for GaAs [47] and Si [105]. It is important to measure and characterize the energy dependence of the deformation potential as it is the key parameter that describes the strength of the electron-acoustic phonon interaction, and defines the upper limit of carrier mobility in a

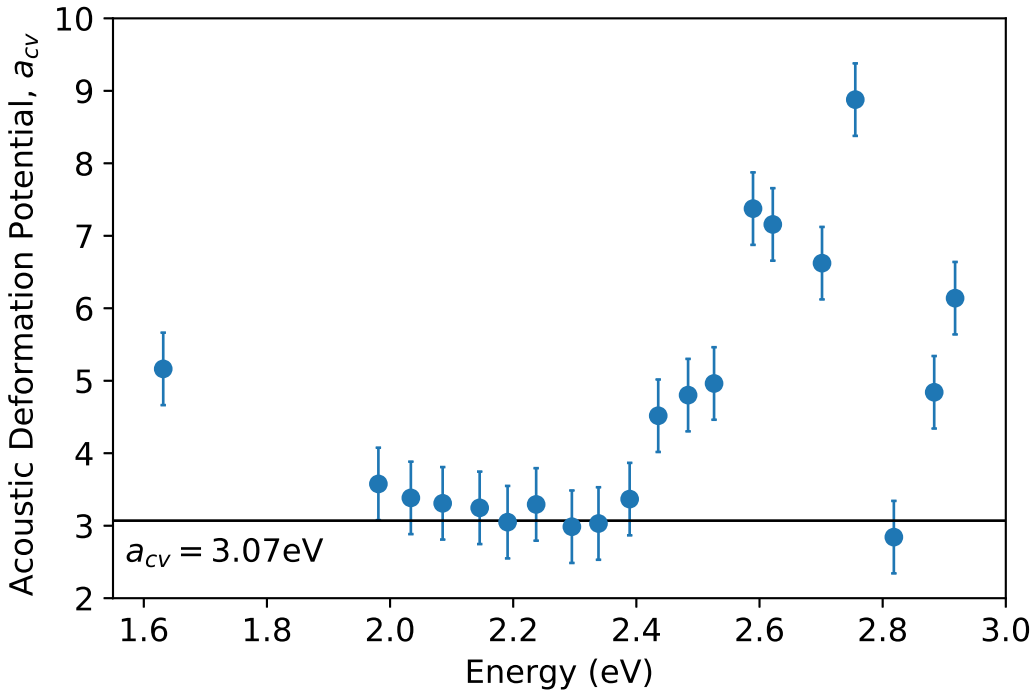

Figure 3.12: Magnitude of the acoustic deformation potential as a function of energy, $|a_{cv}| = 3.07$.

defect free crystal [106]. It has also been found in a theoretical study of bulk GaAs, 3C-SiC and a representative GaAs MESFET structure that in order to simultaneously satisfy the principal transport properties; impact ionization coefficients, average energy, and velocity-filed characteristics, the energy dependence of the acoustic deformation potential has to be taken into account [107].

Chapter 4

Depth dependence of complex refractive index of H^+ implanted 4H-SiC

4.1 Introduction

Silicon carbide (SiC) is a wide band gap semiconductor, ideally suited to high power, high temperature, and high frequency electronic device applications. Recent progress in materials structure and interface passivation has allowed the creation of a useful SiC MOS technology [108]. More recently it has been recognized that isolated defects in SiC can serve as long-lifetime atomic like states suitable for coherent single photon generation and possibly quantum computing structures [17, 18, 19]. Thus, defect creation and defect annealing are important processes associated with these burgeoning SiC technologies. In this letter, we report depth dependent modification of the optical constants of n-type 4H-SiC due to defect creation by hydrogen implantation at 180keV. Optical constants are obtained using coherent acoustic phonon (CAP) spectroscopy. Such knowledge is essential for reliable fabrication of future photonic/optoelectronic devices using silicon carbide. Proton irradiation in space is well known to be responsible for the degradation of satellite's onboard electronics due to radiation damage. Thus, the understanding of the damage (vacancies, interstitials, and their related defects) created by hydrogen implantation is crucial for designing reliable devices for use in space. Hydrogen related defects have been studied for the past decade by electrical techniques (DLTS) [109, 110, 111, 112]. Depth dependent structural damage was probed by RBS and hydrogen profiles by SIMS [113, 114] at implantation fluences above 10^{16} cm^{-2} which defines the sensitivity limits of these tech-

niques. Here, the CAP technique is shown to be two orders of magnitude more sensitive than the channeling probe which is consistent with a previous study [5]. To the best of our knowledge, this is the first time that the CAP technique has been applied to obtain a depth dependent complex refractive index. We used Si-face n-type 4H-SiC ($\rho = 0.7\Omega$·cm) 10 μm epilayers grown on 4H-SiC substrate by a CVD process. Following the fabrication, they were implanted at room temperature with 180 keV hydrogen ions with fluences ranging from 10^{14} to 10^{16} cm^{-2} at 0.9 μA current. No annealing has been carried out following implantation. CAP spectroscopy, also known as picosecond ultrasonics, is a pump probe technique. When an ultrafast high-intensity pump pulse hits an absorbing material it excites electrons that decay into optical and then longitudinal acoustic phonons, which subsequently traverse the material. The CAP wave may be thought of as a crystal strain wave travelling into the solid at the speed of sound. To generate high amplitude coherent acoustic phonons, a thin metal film is typically deposited onto the material surface. Creation of CAP waves can be classically explained by thermal expansion of a metal transducer [115] and the transfer of the elastic wave to the substrate. A delayed probe beam is then reflected both from the surface of the material and from the traveling CAP wave, giving rise to an oscillatory response due to interference between the two reflected beams as shown in Figure 4.1. Using this approach damaged regions at particular depths in the specimen result in a decrease in the signal amplitude and a phase shift in the oscillatory CAP signal with respect to CAP response of the unimplanted specimen. The depth resolution is estimated to be approximately 40 nm based on the CAP wave and probe light pulse widths. In previous studies quantitative defect profiles in He implanted GaAs [35] and also the optical damage cross-section surrounding 400 keV Ne^{++} ion tracks in GaAs were experimentally deter-

mined with high sensitivity [5]. In addition, research on ion-implanted diamond, revealed a fluence-dependent decrease in the real and increase in the imaginary parts of the refractive index as well as a sign reversal in the photoelastic coefficient [36].

4.2 Results and Discussion

In the present experiments, a 10 nm aluminum layer was used as a transducer, deposited using an Angstrom resistive evaporator. CAP measurements were taken using a Coherent Mira 900 Ti:Sapphire laser producing 150-fs pulses at 76 MHz. The pump beam was tuned to 800 nm with 230 mW power and the probe beam was frequency-doubled to 400 nm using BBO crystal with 2 mW power. Both beams were focused onto the specimen with spot diameters of 100 μm and 90 μm for pump and probe, respectively. The pump beam was chopped using an optical chopper at about 3 kHz. The typical pump-probe reflectivity response for both unimplanted and implanted at 10^{16} cm^{-2} fluence specimens is shown in Figure 4.1. Oscillations arising from the traveling CAP wave are superimposed on the thermal response of metal electrons. In the following analysis, the thermal response has been subtracted out, leaving only the CAP oscillations.

The oscillatory part of the reflectivity response measured in CAP spectroscopy can be characterized as [115, 48]

$$\frac{\Delta R(t)}{R_0} \propto A \sin\left(\frac{2\pi t}{T} + \phi\right) e^{-t/\tau} \tag{4.1}$$

where t is time, T is the period, τ is the damping time, and ϕ is the phase. As the CAP wave travels with the speed of sound, the time t can be related to the depth z in the material

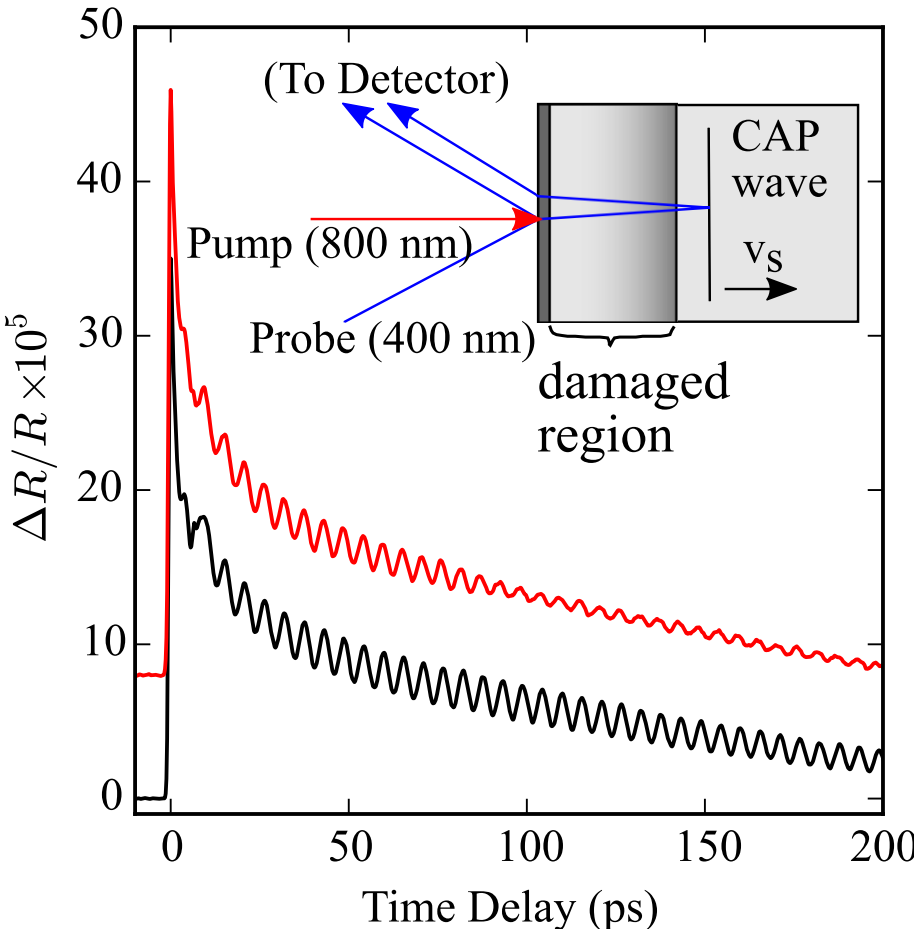

Figure 4.1: Typical CAP responses for implanted (red) at 1×10^{16} cm^{-2} fluence and unimplanted (black) *n*-type 4H-SiC, vertically offset for clarity. Inset: CAP experiment configuration showing strain-wave induced self-interference in the probe reflectivity.

by the equation $z = v_s t$. The oscillation amplitude A is related to the derivatives of real and imaginary parts of the complex refractive index $N = n + i$ with respect to the strain η as shown below

$$A \propto \sqrt{\left(\frac{\partial n}{\partial \eta}\right)^2 + \left(\frac{\partial \kappa}{\partial \eta}\right)^2} \tag{4.2}$$

The period of the oscillation T depends on the real part of refractive index n, speed of sound (CAP wave) v_s, wavelength λ and angle of incidence θ of the probe beam as follows

$$T = \frac{\lambda}{2nv_s \cos\theta} \tag{4.3}$$

The damping time τ is proportional to penetration depth of the probe beam and, consequently, extinction coefficient κ

$$\tau = \frac{\lambda}{4\pi\kappa v_s \cos\theta} \tag{4.4}$$

The measured period and damping time of the CAP oscillations for unimplanted specimen are $T = 5.584$ ps and $\tau = 223.8$ ps, respectively. Using these parameters, we calculate n and κ from equations 4.3 and 4.4 with $= 27$, $v_s = 13.1$ nm/ps and $= 400$ nm to be $n = 3.07$ and $= 0.0122$. These values are in good agreement with previously reported values [116]. Figure 4.2 shows CAP oscillations for specimens implanted at fluences of 10^{14}, 10^{15} and 10^{16} cm^{-2}. Spectra for the implanted specimens are plotted on top of the spectra for the unimplanted specimen. The lattice damage resulting from ion implantation is shown on the top of Figure 4.2. It is estimated from Monte-Carlo simulations performed using the transport of ions in matter (TRIM) code [41].

There is no detectable defect related modification of the CAP signal at 10^{14} cm^{-2} flu-

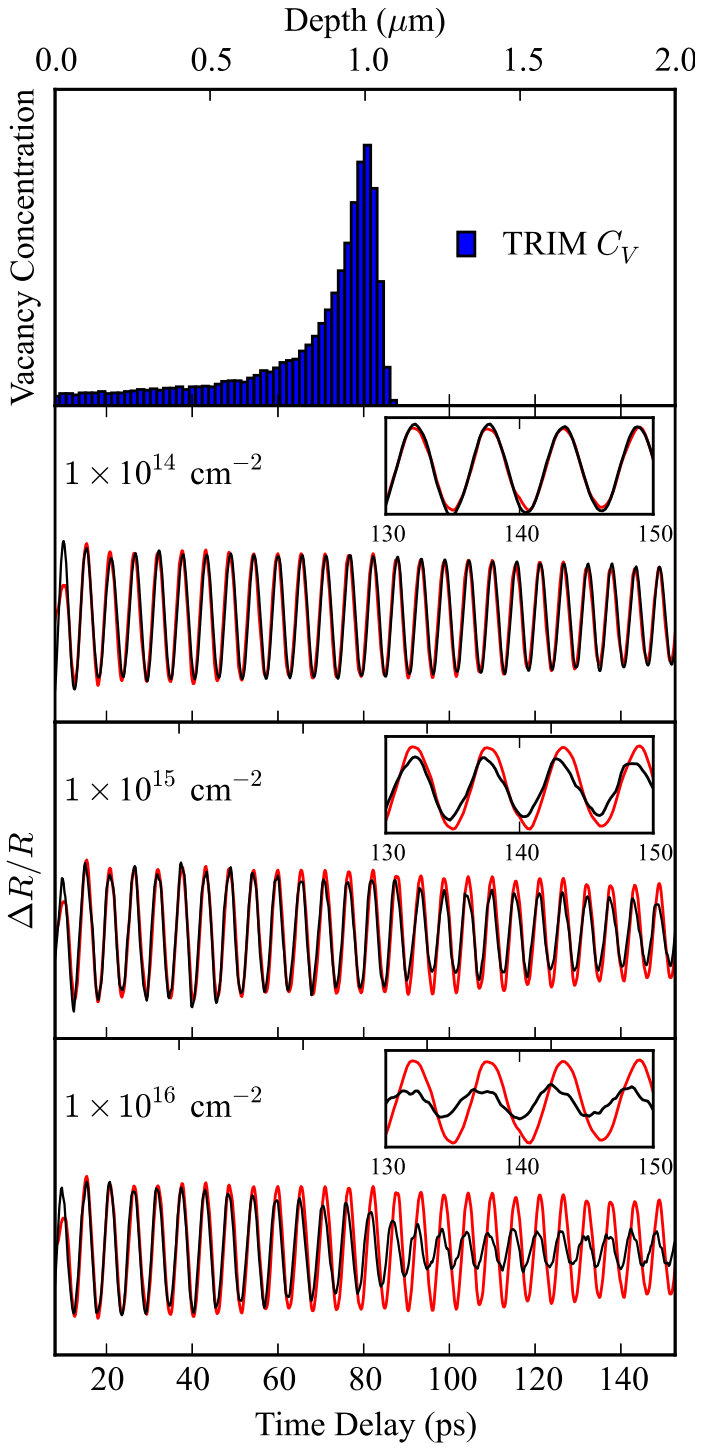

Figure 4.2: CAP oscillations in the pump-probe reflectivity signal of ion-implanted SiC specimens at multiple fluences (black lines). The red line behind each curve is the corresponding response for an unimplanted specimen. Above the CAP responses are the damage-induced vacancy distribution as calculated by the TRIM code. The insets show spectra on the smaller scale to indicate phase shift between two curves.

ence. This defines the sensitivity limit of the CAP technique at this wavelength to H^+ induced optical damage. Two important features of the data are noted for higher implantation fluences. As the implantation fluence increases, the amplitude of the CAP oscillations decreases. This observation is related to the increased absorption of the probe light as expressed in the imaginary part of the complex refractive index arising from the structural damage caused by the hydrogen implantation. Insets in Figure 4.2 show phase shifts of the CAP oscillations in the implanted specimens to the left on the time scale with respect to those in the unimplanted specimens. This can be attributed to an increase in the real part of the complex refractive index of the implanted specimens that results in an increased optical path length for the probe pulse as it travels to the CAP wave and back through damaged SiC lattice as discussed below. As can be seen from the equations 4.1 - 4.4, the CAP oscillatory response primarily depends on the quantities $n, \kappa, \partial n/\partial \eta, \partial \kappa/\partial \eta$. For perfect single crystals, these values are constant as a function of depth. However, ion implantation induces a spatially varying lattice damage profile, which is dependent on depth. The reduction in the oscillatory amplitudes related to the depth dependent implantation damage in SiC lattice may be attributed to (a) modification of the extinction coefficient induced by the lattice defects and/or (b) changes in the derivative terms $\partial(n, \kappa)/\partial \eta$. Figure 4.2 shows an overall cumulative decrease in the amplitude beyond the damaged region that indicates a damage-induced modification of the extinction coefficient. Therefore, in this work, we make an assumption that the derivative terms $\partial(n, \kappa)/\partial \eta$ are constant with respect to the depth in the implanted specimens, i.e. do not contribute to the modulation of the amplitude.

In order to obtain changes in the extinction coefficient $\Delta\kappa$ due to the hydrogen implantation, we divide the envelope of oscillatory signal $\Delta R(z)/R$ corresponding to unimplanted

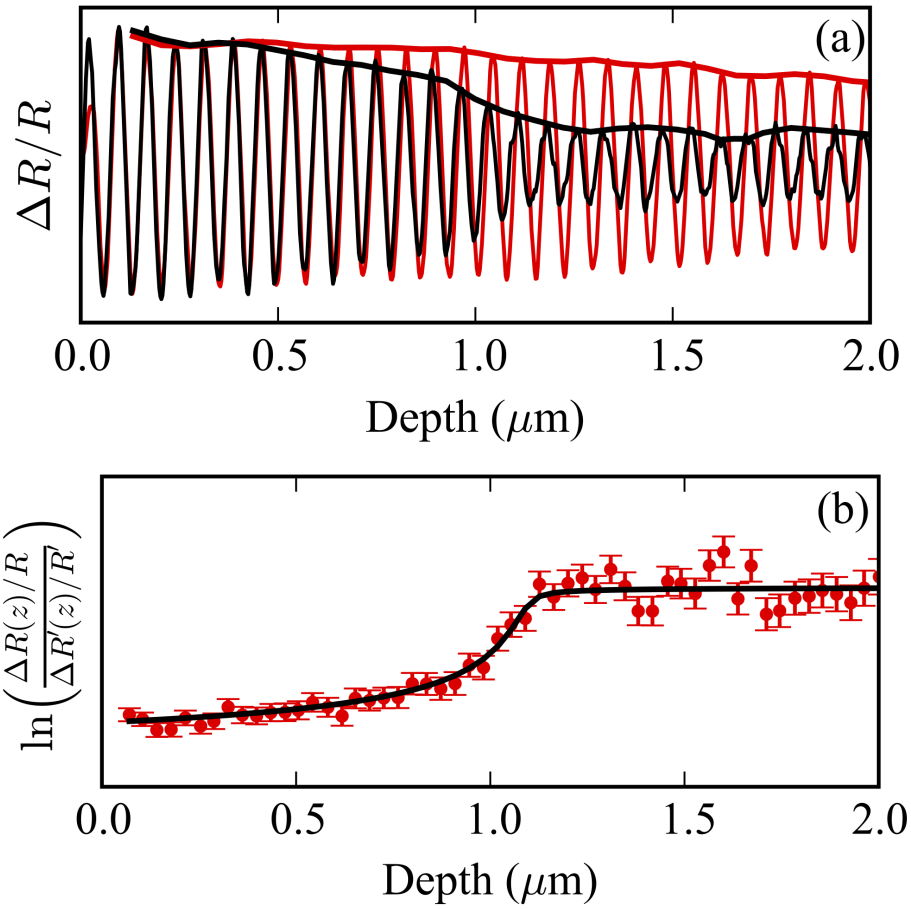

Figure 4.3: a) CAP data obtained at a fluence of 10^{16} cm^{-2} contrasting the implanted/unimplanted data b) Fit of the implanted/unimplanted experimental data using equation 4.5.

specimen by the envelope of oscillatory signal $\Delta R'(z)/R'$ corresponding to implanted specimen (see Figure 4.3a) using formulae 4.1 and 4.4, and after taking the natural logarithm of both sides of the equation, we have

$$\ln\left(\frac{\Delta R(z)/R}{\Delta R'(z)/R'}\right) = \frac{4\pi}{\lambda}\int \Delta\kappa(z')dz' \tag{4.5}$$

By assuming that $\Delta\kappa$ behaves as a Pearson IV function, which is commonly used to describe ion-implanted distributions we fit the parameters of Pearson IV function in the above equation 4.5 to the experimental data (see Figure 4.3b).

Figure 4.4 shows changes in the extinction coefficient $\Delta\kappa(z)$ arising from the 180 keV hydrogen implantation in n-type 4H-SiC at different fluences. Clearly, changes in the extinction coefficient are proportional to the defects densities as estimated by TRIM code. The magnitude of these changes decreases as the implantation fluence decreases. The red curve corresponding to the relatively small fluence of 3×10^{14} cm^{-2} is broadened and shifted due to noise in the CAP spectrum.

It is assumed in this study that the longitudinal speed of sound in the implanted specimens of 4H-SiC is largely unaffected by the implantation induced damage of the lattice. This assumption is supported by the fact that the speed of sound in an amorphous material is shown to be somewhat smaller compared to that in the same type of crystalline material [117, 118]. Thus, a substantial slowing of the speed of sound would result in a phase shift of CAP spectra of the implanted specimen to the right with respect to the spectra of the unimplanted specimen. However, we observe a phase shift in the opposite direction. For this reason, we attribute the observation of the phase shift primarily to an increase in the real part of the refractive index. Thus, the phase shift $\Delta\psi$ between the unimplanted and

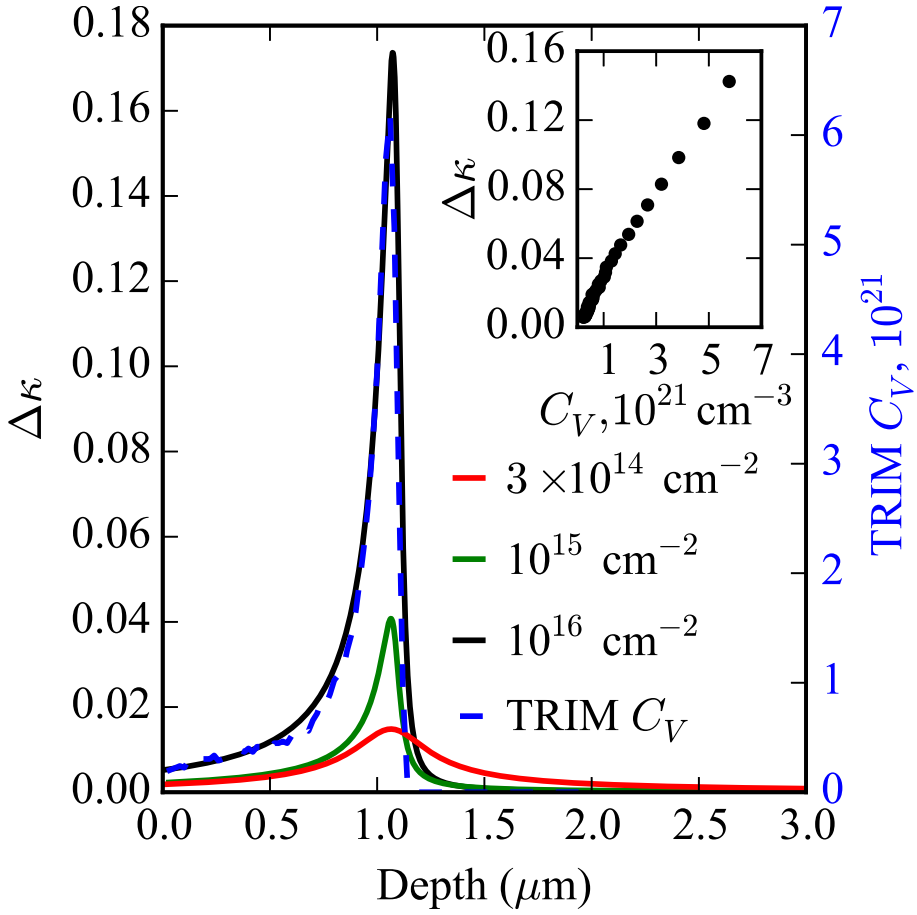

Figure 4.4: Observed changes in the extinction coefficient as a function of depth using CAP, following hydrogen implantation. Dashed line represents TRIM vacancy profile for the highest fluence of the implantation. The inset shows the implantation induced extinction coefficient change versus vacancy concentration calculated from TRIM. The red curve corresponding to the relatively small fluence of 3×10^{14} cm^{-2} is broadened and shifted due noise in the CAP spectrum.

implanted spectrum can be determined as:

$$\Delta\psi = \frac{4\pi\cos\theta}{\lambda}\int \Delta n(z')dz' \tag{4.6}$$

Again, assuming that the change in the real part of the complex refractive index Δn due to the hydrogen implantation behaves as a Pearson IV function we fit above equation 4.6 to the experimental data to obtain depth dependent profiles of the real refractive index change Δn as shown in Figure 4.5. Here, the phase shift was measurable only for the highest dose of implantation.

The implantation-induced change in the real part of the complex refractive index profile is broader and skewed more to the surface side than the vacancy/defect profile calculated by TRIM code. This indicates a nonlinear dependence of modified refractive index on vacancy/defect concentration. The dependence is linear up to a vacancy concentration of about 10^{21} cm^{-3}. In other words, when distances between vacancies are smaller than 10 $\mathring{A}$ (about lattice constant along c-axis) changes in the real part of the complex refractive index due to hydrogen implantation tends to saturate. In comparison, the increase in the real part of the complex refractive index in boron implanted CVD type IIa diamond deviates from linear dependence for vacancy concentrations above 2×10^{21} cm^{-3} [119]. There have been previous studies of damage arising from ion implantation leading to changes in the refractive index in a variety of optical materials. It was observed for many of those materials that changes in the refractive index Δn arise mostly from changes in local volume *DeltaV* [1]. However, there are other defect-dependent parameters that can contribute to refractive index change such as the atomic bond polarizability α and the structure factor F. These

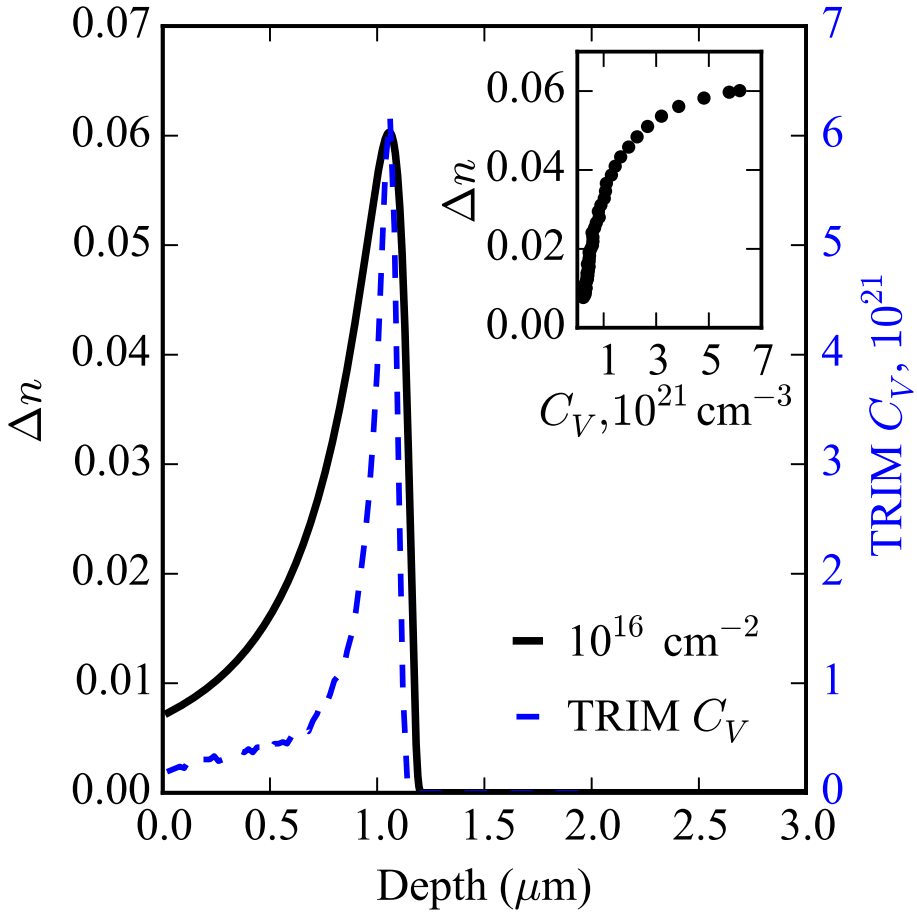

Figure 4.5: Observed changes in the refractive index as a function of depth using CAP, following hydrogen implantation. The dashed line represents the TRIM vacancy profile for the highest implantation fluence, 10^{16} cm^{-2}. The inset shows the implantation induced refractive index change versus vacancy concentration calculated from TRIM.

factors are embodied in the Wei adaptation of the Lorentz-Lorenz equation [120, 121, 122]:

$$\frac{\Delta n}{n} = \frac{(n^2-1)(n^2+2)}{6n^2}\left[-\frac{\Delta V}{V} + \frac{\Delta \alpha}{\alpha} + F\right]. \tag{4.7}$$

For the case of silicon carbide, volume expansion of the damaged region was observed [123, 124], which if treated as the only factor would result in a decrease in the refractive index. However, in the present work an increase in n and was observed as the defect concentration increases. We postulate that the observed increase in the refractive index n is due to contributions from the atomic bond polarizability α and/or structure factor F. Thus, ionization from electronic stopping is likely to be a major contributing factor leading to an increase in the real part of the complex refractive index. Further work is needed to determine the relative contributions of these and possibly other parameters. It is interesting to compare these results to the studies of the index change with ion bombardment in similar covalently bonded materials. For examples, several studies report increased refractive index arising from ion implantation in diamond [125, 126, 119, 127, 128], silicon [129, 130, 131, 132] and germanium [133] despite considerable volume expansion. In all cases, the increase is attributed to a change in the atomic bond polarizability. Thus, this new report of the change in index with ion bombardment adds one more significant point to the body of data that relate the large change in polarizability with ion bombardment for covalent semiconductors.

4.3 Conclusion

In conclusion, we have measured depth-dependent profiles of optical constants arising from hydrogen ion implantation at low doses in *n*-type 4H-SiC using coherent acoustic phonon spectroscopy. CAP spectroscopy is shown to be a sensitive non-destructive tool for studying the implantation damage-induced modification of the opto-electronic nature of silicon carbide lattice. Our results show a strong dependence of the 4H-SiC complex refractive index as a function of depth and H^+ fluence. We note also that the implantation-modified refractive index (real part) profile is broader and skewed toward the surface as compared to the implantation induced structural damage profile, predicted by Monte Carlo calculations. This increase in the real part of the refractive index may be accounted for by invoking changes in the atomic bond polarizability arising from ionization due to electronic stopping during implantation. Both real and imaginary parts of the complex refractive index are observed to increase as a function of defect density. These studies provide insight into the influence of defects on optical properties of relevance to the fabrication of SiC-based waveguides and other photonic and optoelectronic devices.

Chapter 5

The photoelastic coefficient of H^+ implanted GaAs as a function of defect density

5.1 Introduction

The photoelastic effect describes the coupling between light and sound in terms of the overall intensity and polarization properties of light scattering[134]. This effect has been applied to study stress distribution in semiconductor systems and lattice-mismatched semiconductor heterostructures. Its practical importance has been found in many optoelectronic devices such as light modulators, deflectors, and switches[135]. The knowledge of the photoelastic tensor is crucial for the proper design of cavity optomechanical systems[136, 137]. Gallium arsenide (GaAs) is a semiconductor of the utmost importance for optoelectronics. Due to its relatively large photoelastic coefficients[138], it is used for optomechanical resonators[137]. However, it is necessary to understand the influence of defects on the photoelastic coefficients in solids for reliable device fabrication. Defects, the origin of disorder, can be introduced into a specimen in various ways, e.g. during either materials growth, device fabrication processes or operation in harsh environments. Determining specifics of the relationship between structural disorder and basic optical properties, such as the complex refractive index and the photoelastic coefficients, is the key to understand the behavior of materials that have some amount of disorder. Proton (H^+) irradiation in space is well known to be responsible for the degradation of satellite's on-board electronics due to radiation damage[139, 140, 141]. Thus, understanding the damage (vacancies, interstitials, and their related defects) created by hydrogen implantation is crucial for designing reliable

devices for use in space.

In this paper, we report depth profile and defect density dependence of the relative changes in the photoelastic coefficient P_{12} caused by H^+ implantation in GaAs (100). The depth dependent profile is obtained using the time-domain Brillouin scattering (TDBS) technique. This technique is also known as picosecond ultrasonics or coherent acoustic phonon (CAP) spectroscopy. It has already been applied to study properties of intrinsic GaAs[142, 143, 144, 145, 89, 146]. Other experimental techniques such as stress induced birefringence, Brillouin scattering, and ellipsometry under uniaxial stress can only provide averaged bulk values of the photoelastic coefficients. TDBS, on the other hand, has been widely used to access depth dependent material properties such as elastic and optical inhomogeneities in disordered films[25, 26, 27], ion implantation induced modification of interfacial bonding[28], sub-μm textures in materials compressed at megabar pressures[29, 30], doping profiles[31], distribution of stress[32], imaging of grain microstructure[33], and determination of laser-induced temperature gradients in liquids[34]. Recently, we applied this technique to determine depth profiles of the complex refractive index modification arising from H^+ implantation in 4H-SiC[49]. Point defect concentration profiles and optical damage cross-sections were obtained in He^{++}[35] and Ne^{++}[5] implanted GaAs, respectively. The application of TDBS to He^{++} implanted diamond revealed fluence dependent changes in the complex refractive index and sign reversal of the photoelastic coefficient P_{12}[36]. To the best of our knowledge, there is no other non-destructive technique capable of measuring depth dependent changes in photoelastic coefficients with high resolution. In general, the field of ion implanted semiconductors suffers from a lack of knowledge of the dependence of photoelastic coefficients on defect density.

5.2 Results and Discussion

Time-domain Brillouin scattering, also known as picosecond ultrasonics, is a pump-probe technique. Picosecond ultrasonics has been thoroughly reviewed by Matsuda et al.[88]. An incoming femtosecond pump pulse generates a coherent acoustic phonon wave which is a picosecond strain wave traversing the material at the speed of sound. To facilitate the generation of high amplitude coherent acoustic phonons, a thin metal film is typically deposited onto the material surface. For our experiments, a titanium layer of 20 nm was deposited using e-beam evaporation. The acoustic impedance mismatch between Ti and GaAs is negligible in that it ensures CAP wave transfer from Ti to GaAs without reflection at the interface. Generation of CAP waves in the metallic transducer can be classically explained by thermal expansion [115]. A time-delayed probe beam is then reflected both from the surface of the material and from the traveling CAP wave, giving rise to Brillouin oscillations due to interference between two reflected beams. The oscillation amplitude and frequency are dependent on material properties. Therefore, the damaged region in the ion implanted specimen will result in a different oscillatory signal compared to the unimplanted specimen. The Brillouin oscillations are always superimposed on the thermal response of the metallic transducer. In the following analysis, the thermal background has been subtracted out, leaving only the oscillatory part of the signal. Figure 5.1 shows Brillouin oscillations for unimplanted (red) and implanted (black) GaAs specimens at 3×10^{15} cm^{-2} fluence for different probe polarizations. The damage-induced vacancy distribution calculated by the transport of ions in matter (TRIM) code[41] is shown at the top of Figure 5.1. The important observation to be derived from this data is that the oscil-

lation amplitude decreases in the damaged region as indicated by the vacancy profile while the period and phase remain identical over the entire time (and thus, depth) window for both specimens. The reduction in oscillation amplitude cannot be attributed to the changes in the complex refractive index or speed of sound. Changes in the complex refractive index and speed of sound will result in the cumulative changes in the oscillation amplitude and period passed the damage region. It is seen in Figure 5.1 that the oscillation amplitude of the implanted specimen becomes congruent with that of the unimplanted specimen passed the damaged region. Therefore, the modulation of the oscillation amplitude in the damaged region can be entirely attributed to the changes in the derivative terms of optical constants $\partial n/\partial\eta, \partial\kappa/\partial\eta$[115], and consequently to the photoelastic coefficients P_{12} and P_{11}. The difference in the oscillation amplitude in the damaged region for s- and p-polarization of the probe beam arises from different photoelastic contributions to the oscillation amplitude (see Fig. 5.1). This observation is discussed in detail in the next section.

Following the derivation of transient reflectivity for a two layer system with oblique incident probe light by Matsuda and Wright[92], the perturbation in dielectric constant $\varepsilon_{pe}(z,t)$ in isotropic material (such as GaAs) depends on the strain $\eta_{zz}(z,t)$ and photoelastic tensor components P_{11} and P_{12} (that are depth dependent in our case due to the damage

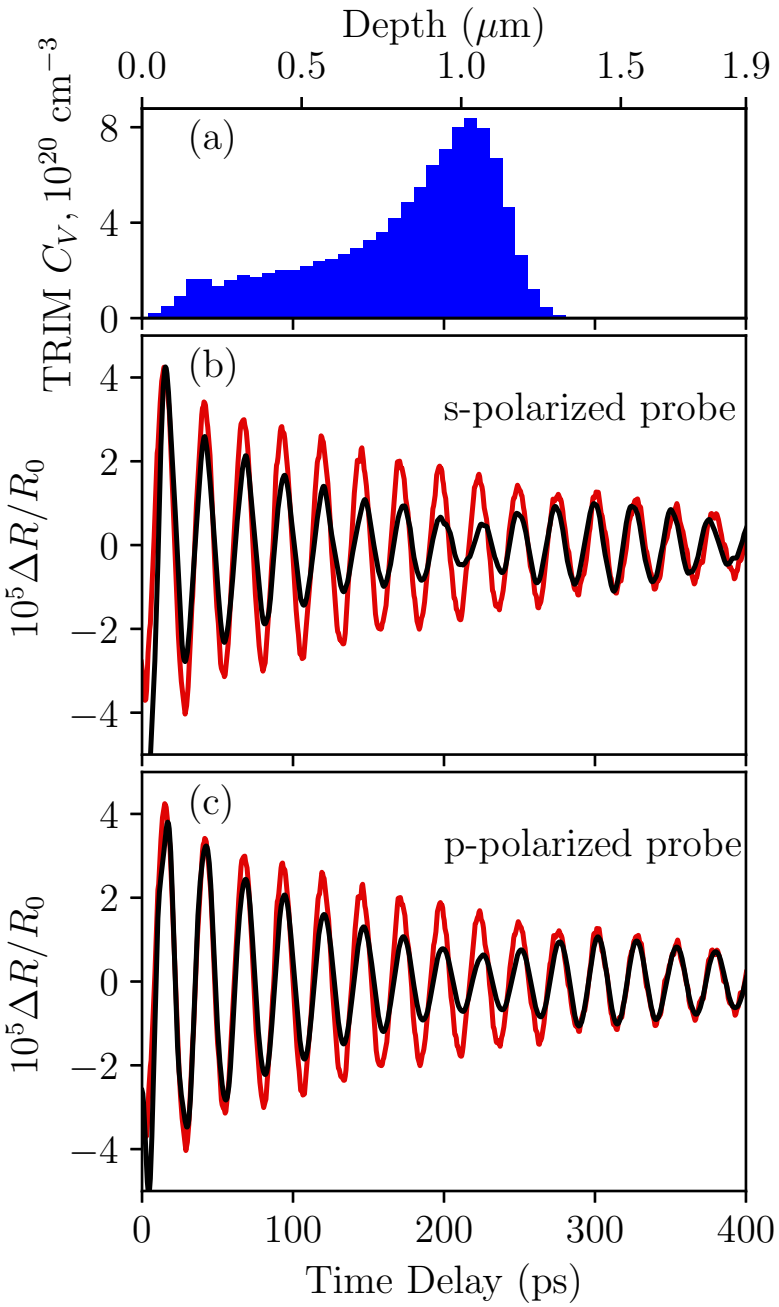

Figure 5.1: The damage-induced vacancy distribution as calculated by the TRIM code is shown in (a). Brillouin oscillations in the pump-probe reflectivity signal of the H^+ implanted GaAs specimens for (b) s- and (c) p-polarized probe beam (in black). The probe wavelength is 880 nm. The implantation fluence is 3×10^{15} cm^{-2}. Red curves represent the corresponding signal for an unimplanted specimen.

arising from H^+ implantation) as

$$\varepsilon_{pe}(z,t) = \begin{pmatrix} P_{12}^{(j)}(z) & 0 & 0 \\ 0 & P_{12}^{(j)}(z) & 0 \\ 0 & 0 & P_{11}^{(j)}(z) \end{pmatrix} \eta_{zz}(z,t), \tag{5.1}$$

where index j indicates layer number. Any changes in the complex refractive index are negligible as discussed in the previous section, and thus its value is constant with respect to the depth coordinate, z. The speed of the CAP wave does not change in the implanted region because our data does not show a phase shift between the oscillatory signals corresponding to implanted and unimplanted specimens. Thus, the complex reflectance change for s- and p-polarized light is then given by [92]:

$$\begin{aligned} \frac{\delta r^{(s)}}{r^{(s)}} = \frac{2k^2}{2k_0 a_0^{(s)} b_0^{(s)}} \Bigg[& \int_0^d \eta(z',t)\left(a_1^{(s)} e^{ik_1 z'} + b_1^{(s)} e^{-ik_1 z'}\right)^2 dz' \\ & + \int_0^\infty P_{12}^{(2)}(z')\eta(z'+d,t)\left(a_2^{(s)} e^{ik_2 z'}\right)^2 dz' \\ & + u(0,t)(1-\varepsilon_1)\left(a_1^{(s)} + b_1^{(s)}\right)^2 + u(d,t)(\varepsilon_1 - \varepsilon_2)\left(a_2^{(s)}\right)^2 \Bigg], \end{aligned} \tag{5.2}$$

$$\frac{\delta r^{(p)}}{r^{(p)}} = \frac{i}{2k_0 a_0^{(p)} b_0^{(p)}} \Bigg[\frac{k_1^2}{\varepsilon_1} P_{12}^{(1)} \int_0^d \eta(z',t) \left(a_1^{(s)} e^{ik_1 z'} + b_1^{(s)} e^{-ik_1 z'} \right)^2 dz'$$

$$+ \frac{k_x^2}{\varepsilon_1} P_{11}^{(1)} \int_0^d \eta(z',t) \left(a_1^{(s)} e^{ik_1 z'} - b_1^{(s)} e^{-ik_1 z'} \right)^2 dz'$$

$$+ \int_0^\infty \frac{k_2^2 P_{12}^{(2)}(z') - k_x^2 P_{11}^{(2)}(z')}{\varepsilon_2} \eta(z'+d,t) \left(a_2^{(p)} e^{ik_2 z'} \right)^2 dz' \tag{5.3}$$

$$+ u(0,t)(1-\varepsilon_1) \left\{ \frac{k_1^2}{\varepsilon_1} \left(a_1^{(p)} + b_1^{(p)} \right)^2 - k_x^2 \left(a_1^{(p)} - b_1^{(p)} \right)^2 \right\}$$

$$+ u(d,t)(\varepsilon_1 - \varepsilon_2) \left(\frac{k_2^2}{\varepsilon_2} - \frac{k_x^2}{\varepsilon_1} \right) \left(a_2^{(s)} \right)^2 \Bigg],$$

where $r^{(\mu)} = b_{(0)}^{(\mu)} / a_{(0)}^{(\mu)}$ is the reflectance for the unperturbed (by the strain wave) sample, d is the thickness of the transducer layer, $k_j = \sqrt{\varepsilon_j k^2 - k_x^2}$ is the wave vector in j-th medium, k is the wave vector in vacuum, a_j and b_j are the electric field amplitudes in j-th layer, u is the displacement, ε_1 and ε_2 are dielectric constants of the transducer and the substrate, respectively[92]. The first term in equation (5.2) and first two terms in equation (5.3) describe contribution to the reflectivity change when the strain wave is traveling through the transducer layer, once it leaves the layer, these terms vanish. We ignore any contribution from the static strain caused by elevated temperature of the transducer layer. Terms that include displacement of the surface and the interface, $u(z,t) = \int_{-\infty}^{z} \eta(z',t) dz'$, also vanish when the strain wave is transmitted to GaAs. Therefore, we can rewrite equations (5.2) and (5.3) as following

$$\frac{\delta r^{(s)}}{r^{(s)}} = \frac{2k^2}{2k_0 a_0^{(s)} b_0^{(s)}} \int_0^\infty P_{12}^{(2)}(z') \eta(z'+d,t) \left(a_2^{(s)} e^{ik_2 z'} \right)^2 dz', \tag{5.4}$$

$$\frac{\delta r^{(p)}}{r^{(p)}} = \frac{i}{2k_0 a_0^{(p)} b_0^{(p)}} \int_0^{\infty} \frac{k_2^2 P_{12}^{(2)}(z') - k_x^2 P_{11}^{(2)}(z')}{\varepsilon_2} \eta(z'+d,t)\left(a_2^{(p)} e^{ik_2 z'}\right)^2 dz'. \tag{5.5}$$

For the implanted specimen, we can make an assumption that the components of the photoelastic tensor are slowly varying functions and therefore can be assumed to be constant for the width of the strain pulse, which is estimated to be of the order of 30 nm for the Ti/GaAs structure. Thus, we can take $P_{12}(z)$ and $P_{11}(z)$ out of the integral

$$\frac{\delta r^{(s)}}{r^{(s)}} = \frac{2k^2}{2k_0 a_0^{(s)} b_0^{(s)}} P_{12}^{(2)}(v_s t) \int_0^{\infty} \eta(z'+d,t)\left(a_2^{(s)} e^{ik_2 z'}\right)^2 dz', \tag{5.6}$$

$$\frac{\delta r^{(p)}}{r^{(p)}} = \frac{i}{2k_0 a_0^{(p)} b_0^{(p)}} \frac{k_2^2 P_{12}^{(2)}(v_s t) - k_x^2 P_{11}^{(2)}(v_s t)}{\varepsilon_2} \int_0^{\infty} \eta(z'+d,t)\left(a_2^{(p)} e^{ik_2 z'}\right)^2 dz'. \tag{5.7}$$

If we write equations (5.6) and (5.7) for both implanted and unimplanted specimens, then subtract implanted from unimplanted and divide by unimplanted, we obtain

$$\frac{\left(\delta r^{(s)}/r^{(s)}\right)_U - \left(\delta r^{(s)}/r^{(s)}\right)_I}{\left(\delta r^{(s)}/r^{(s)}\right)_U} = \frac{\left[P_{12}^{(2)}\right]_U - \left[P_{12}^{(2)}(v_s t)\right]_I}{\left[P_{12}^{(2)}\right]_U} \equiv -\frac{\Delta P_{12}}{P_{12}}, \tag{5.8}$$

$$\frac{\left(\delta r^{(p)}/r^{(p)}\right)_U - \left(\delta r^{(p)}/r^{(p)}\right)_I}{\left(\delta r^{(p)}/r^{(p)}\right)_U} = \frac{\left[P_{eff}^{(2)}\right]_U - \left[P_{eff}^{(2)}(v_s t)\right]_I}{\left[P_{eff}^{(2)}\right]_U} \equiv -\frac{\Delta P_{eff}}{P_{eff}}, \tag{5.9}$$

where $P_{eff}^{(2)} = \left[k_2^2 P_{12}^{(2)} - k_x^2 P_{11}^{(2)}\right]/\varepsilon_2$, indices U and I represent unimplanted and implanted specimens, respectively.

By processing the amplitudes of the Brillouin oscillations for implanted and unimplanted specimens according to equations (5.8) and (5.9), we obtain the relative changes in the photoelastic coefficients with respect to the depth for H^+ implanted GaAs. As seen

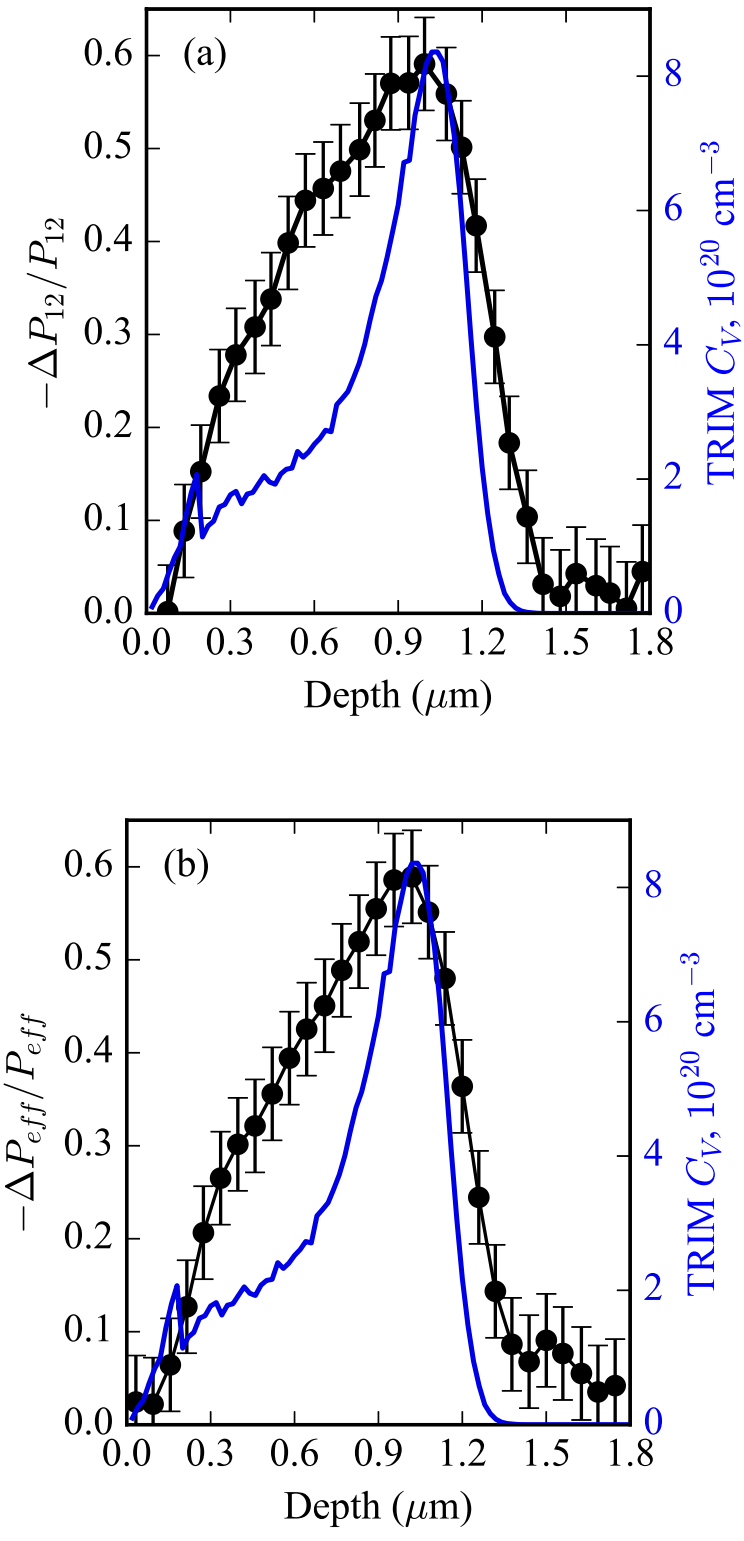

Figure 5.2: Depth dependent profiles of the relative changes in the photoelastic coefficients $\Delta P_{12}/P_{12}$ (a) and $\Delta P_{eff}/P_{eff}$ (b) of GaAs implanted at 3×10^{15} cm^{-2} with 140 keV H^+. The error bars were estimated from statistical analysis of a set of experimental spectra.

in Figure 5.2, the profiles of the relative changes in the photoelastic coefficients show two regimes in depth: from 0μm to 0.2μm they follow the vacancy profile and from 0.2μm to 1μm they reveal different trend (it is broader) than that of the vacancy profile as obtained from the the TRIM code simulations. This fact indicates a nonlinear dependence of modified photoelastic coefficients on vacancy/defect concentration. The effect on the photoelastic properties due to ion implantation extends much further than the structural damage.

The peak of the relative changes of both photoelastic coefficients $\Delta P_{12}/P_{12}$ and $\Delta P_{eff}/P_{eff}$ is about 60%. ΔP_{11} has a factor k_x^2 in the definition of ΔP_{eff} whereas ΔP_{12} has a factor of k_2^2. In our case, $k_x^2 << k_2^2$ that results in small contribution of P_{11} to P_{eff}. Thus, we were not able to extract $\Delta P_{11}/P_{11}$ from $\Delta P_{eff}/P_{eff}$ because any difference between $\Delta P_{12}/P_{12}$ and $\Delta P_{eff}/P_{eff}$ are on the order of the noise present.

Figure 5.3 shows the dependence of the relative changes in the photoelastic coefficient P_{12} with respect to the vacancy concentration. It is obtained by dividing the relative changes in the photoelastic coefficient P_{12} by corresponding vacancy concentration as predicted by the TRIM code. As defect density (vacancy concentration) increases, the change in the photoelastic coefficient also increases towards its saturation value.

A. Steigerwald et al.[5] have estimated optical constants (n and κ) and their derivatives ($\partial n/\partial E$ and $\partial \kappa/\partial E$) with respect to defect concentrations in disordered GaAs crystal using phenomenological band structure calculations. Their model assumes isolated, randomly placed point defects, which is an oversimplification of the clustered defect configurations one usually assumes with ion implantation damage. However, it has an advantage to study disordered systems at a low computational cost. The photoelastic coefficient P_{12}

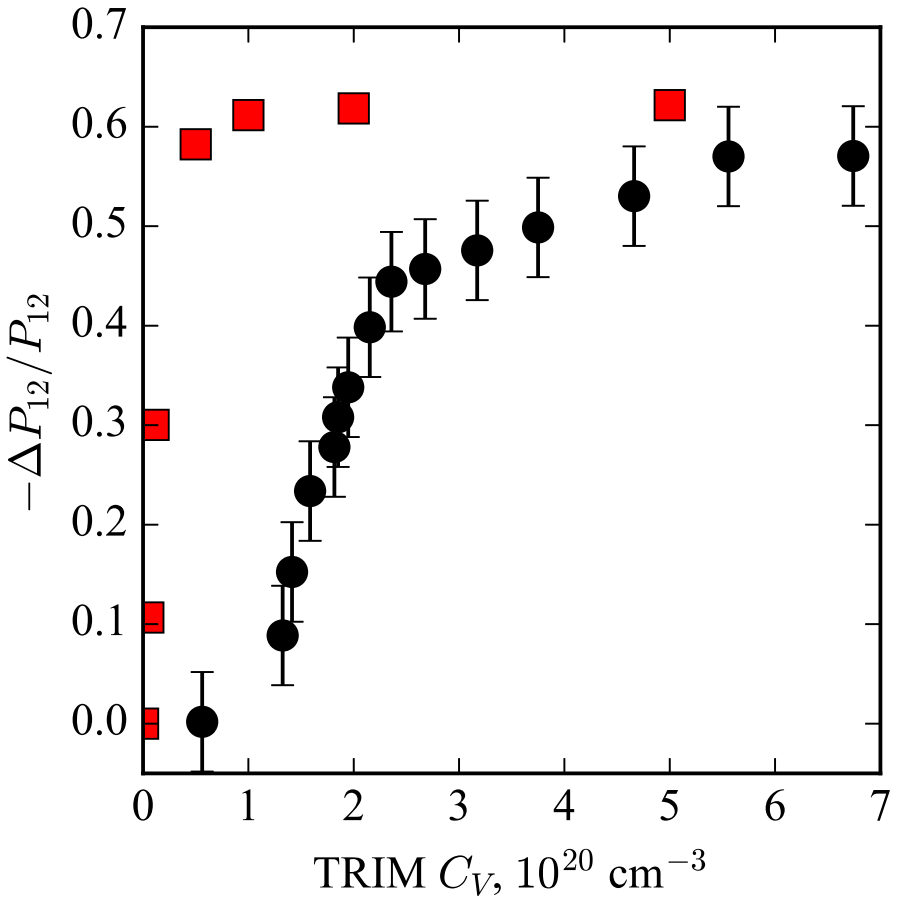

Figure 5.3: Black circles represent the relative changes in the photoelastic coefficient P_{12} with respect to vacancy concentration. Red squares represent calculated values for the relative changes in the photoelastic coefficient P_{12} as a function of vacancy concentration derived from a previous study [5].

is propotional to the strain derivatives of the optical constants as

$$P_{12} \propto \sqrt{\left[\frac{\partial n}{\partial E}\right]^2 + \left[\frac{\partial \kappa}{\partial E}\right]^2} \frac{\partial E}{\partial \eta}, \tag{5.10}$$

where $\partial(n, \kappa)/\partial E$ is the rate of the change in the refractive index versus photon frequency, and $\partial E/\partial \eta$ is a deformation potential. Thus, by using equation (5.10) and the values of derivatives $\partial n/\partial E$, $\partial \kappa/\partial E$ from the reference [5], we obtain several theoretical data points for our range of vacancy concentrations. These points are presented in Figure 5.3 as red squares. The relative changes in the photoelastic coefficient P_{12} obtained by the simple phenomenological model [5] follow a trend similar to the experimental data but the calculated model dependent changes in the photoelastic coefficient are overestimated at lower defect densities as seen in Figure 5.3. This disagreement may be explained by the fact that the model is based on isolated point defects and does not account for any clustered defect configurations.

5.3 Conclusion

In conclusion, we have demonstrated that TDBS can be applied to measure depth profiles of photoelastic coefficients in hydrogen ion bombarded GaAs. The method proposed here is suitable only for low fluences of implantation (low structural damage) because at higher implantation doses, changes in the complex index of refraction and sound velocity may occur. In the case when two or more quantities (refractive index, speed of sound, photoelastic coefficients) depend on a depth coordinate; a theory incorporating all depth

dependent quantities such as developed by V. Gusev et. al.[26] should be applied. Experimental results for H^+ implanted GaAs show that the implantation damage induced changes in the photoelastic coefficient P_{12} increase non-linearly with vacancy concentration. The absolute value of the photoelastic coefficient P_{12} decreases in damaged GaAs. Its depth profile is broader than the depth distribution of defects as predicted by the TRIM code. This indicates that the optical damage extends further than the structural damage, which is similar to the effect of GaAs implantation with other ions[35, 5]. The experimental results obtained in this work are of significant importance to the theory of the photoelasticity of disordered semiconductors as well as for the GaAs based elastooptic devices operating in harsh environments or subjected to unintended defect creation during fabrication.

5.4 Methods

Sample preparation

GaAs (100) sample was implanted at room temperature with 140 keV hydrogen ions at 3×10^{15} cm^{-2} fluence and 0.85 μA current. No annealing was carried out following the implantation. In order to perform time-domain Brillouin scattering, a 20 nm titanium layer was deposited using Angstrom e-beam evaporator at 2 Å/s deposition rate to serve as a transducer for CAP wave. The choice of Ti is supported by the excellent acoustic impedance matching with GaAs (8%) that suppresses acoustic reflection at their interface.

Time-domain Brillouin scattering

Time-domain Brillouin scattering measurements were performed in a standard time-resolved pump-probe setup in reflection geometry. A Coherent Mira 900 with 150-fs pulses at 76 MHz was used as a laser source. The pump and probe beams were tuned to 880 nm with 200 mW power and 10 mW power, respectively. Angle of incidence of the probe beam was 30°. The probe wavelength is tuned to the band edge of GaAs because of high sensitivity to implantation damage[5]. Both beams were focused onto the specimen with spot diameters of 100 μm and 90 μm for pump and probe, respectively. The pump beam was chopped using Thorlabs optical chopper at about 3 kHz.

Chapter 6

Conclusions and outlook

In conclusion, we have studied the deformation potential of gallium phosphide as well as the optical and elasto-optical effects of H^+ ion implantation in 4H-SiC and GaAs by means of time-domain Brillouin scattering.

Specifically, in Chapter 3 we have shown how the acoustic deformation potential can be measured using time-domain Brillouin scattering. Our results indicate strong energy dependence of the deformation potential above the indirect band gap of gallium phosphide. The deformation potential reaches peak at the Γ point and increases towards the L point. Similar behaviour in the amplitude of Brillouin oscillations have been observed for GaAs [47] and Si [105]. It is important to measure and characterize the energy dependence of the deformation potential as it is the key parameter that describes the strength of the electron-acoustic phonon interaction, and defines the upper limit of carrier mobility in a defect free crystal [106]. It has also been found in a theoretical study of bulk GaAs, 3C-SiC and a representative GaAs MESFET structure that in order to simultaneously satisfy the principal transport properties; impact ionization coefficients, average energy, and velocity-filed characteristics, the energy dependence of the acoustic deformation potential has to be taken into account [107].

In Chapter 4, we have measured depth-dependent profiles of optical constants arising from hydrogen ion implantation at low doses in *n*-type 4H-SiC. Time-domain Brillouin scattering is shown to be a sensitive non-destructive tool for studying the implantation

damage-induced modification of the opto-electronic nature of silicon carbide lattice. Our results show a strong dependence of the 4H-SiC complex refractive index as a function of depth and H^+ fluence. We note also that the implantation-modified refractive index (real part) profile is broader and skewed toward the surface as compared to the implantation induced structural damage profile, predicted by Monte Carlo calculations. This increase in the real part of the refractive index may be accounted for by invoking changes in the atomic bond polarizability arising from ionization due to electronic stopping during implantation. Both real and imaginary parts of the complex refractive index are observed to increase as a function of defect density. These studies provide insight into the influence of defects on optical properties of relevance to the fabrication of SiC-based waveguides and other photonic and optoelectronic devices.

In Chapter 5, we have demonstrated that time-domain Brillouin scattering can be applied to measure depth profiles of photoelastic coefficients in hydrogen ion bombarded GaAs. The method proposed here is suitable only for low fluences of implantation (low structural damage) because at higher implantation doses, changes in the complex index of refraction and sound velocity may occur. In the case when two or more quantities (refractive index, speed of sound, photoelastic coefficients) depend on a depth coordinate; a theory incorporating all depth dependent quantities such as developed by V. Gusev et. al.[26] should be applied. Experimental results for H^+ implanted GaAs show that the implantation damage induced changes in the photoelastic coefficient P_{12} increase non-linearly with vacancy concentration. The absolute value of the photoelastic coefficient P_{12} decreases in damaged GaAs. Its depth profile is broader than the depth distribution of defects as predicted by the TRIM code. This indicates that the optical damage extends further than

the structural damage, which is similar to the effect of GaAs implantation with other ions [35, 5]. The experimental results obtained in this work are of significant importance to the theory of the photoelasticity of disordered semiconductors as well as for the GaAs based elastooptic devices operating in harsh environments or subjected to unintended defect creation during fabrication.

Future studies

Further development and application of time-domain Brillouin scattering to study ion matter interactions suggests the following potential research projects:

(i) Color centers in wide band gap semiconductors (NV^- center in diamond and SiV centers in SiC, for example) are promising for many quantum information application. However, there are still challenges in this field in determining the precise depth positions of color centers to further develop deterministic ion placement. Time-domain Brillouin scattering holds a great promise for addressing this issue by tuning the probe wavelength to the absorption lines of specific defects.

(ii) Another exciting direction is to utilize picosecond strain wave to control electronic energy levels [59] of color centers. That may allow, for example, to shift the emission lines of single-photon emitters on a picosecond timescale.

BIBLIOGRAPHY

[1] Peter David Townsend, PJ Chandler, and L Zhang. *Optical effects of ion implantation*, volume 13. Cambridge University Press, 2006.

[2] W. K. Hofker, D. P. Oosthoek, N. J. Koeman, and H. A. M. de grefte. Concentration profiles of boron implantations in amorphous and polycrystalline silicon. *Radiation Effects*, 24(4):223–231, 1975.

[3] Mikhail N. Polyanskiy. Refractive index database. https://refractiveindex.info. Accessed on 2018-02-01.

[4] Kunie Ishioka, Avinash Rustagi, Ulrich Höfer, Hrvoje Petek, and Christopher J. Stanton. Intrinsic coherent acoustic phonons in the indirect band gap semiconductors Si and GaP. *Physical Review B*, 95(3):035205, jan 2017.

[5] A. Steigerwald, A. B. Hmelo, K. Varga, L. C. Feldman, and N. Tolk. Determination of optical damage cross-sections and volumes surrounding ion bombardment tracks in GaAs using coherent acoustic phonon spectroscopy. *J. Appl. Phys.*, 112(1):013514, jul 2012.

[6] I. M. Tiginyanu, C. Schwab, J.-J. Grob, B. Prvot, H. L. Hartnagel, A. Vogt, G. Irmer, and J. Monecke. Ion implantation as a tool for controlling the morphology of porous gallium phosphide. *Applied Physics Letters*, 71(26):3829–3831, 1997.

[7] M. A. Capano, S. Ryu, M. R. Melloch, J. A. Cooper, and M. R. Buss. Dopant activation and surface morphology of ion implanted 4H- and 6H-silicon carbide. *Journal of Electronic Materials*, 27(4):370–376, apr 1998.

[8] T Hioki, A Itoh, M Ohkubo, S Noda, H Doi, J Kawamoto, and O Kamigaito. Mechanical property changes in sapphire by nickel ion implantation and their dependence on implantation temperature. *Journal of materials science*, 21(4):1321–1328, 1986.

[9] Baojian Liu, Bin Deng, and Ye Tao. Influence of niobium ion implantation on the microstructure, mechanical and tribological properties of tialn/crn nano-multilayer coatings. *Surface and Coatings Technology*, 240:405–412, 2014.

[10] A Meldrum, LA Boatner, and CW White. Nanocomposites formed by ion implantation: Recent developments and future opportunities. *Nuclear Instruments and Methods in Physics Research Section B: Beam Interactions with Materials and Atoms*, 178(1-4):7–16, 2001.

[11] R Lopez, LA Boatner, TE Haynes, RF Haglund Jr, and LC Feldman. Enhanced hysteresis in the semiconductor-to-metal phase transition of vo 2 precipitates formed in sio 2 by ion implantation. *Applied Physics Letters*, 79(19):3161–3163, 2001.

[12] DP Norton, SJ Pearton, AF Hebard, N Theodoropoulou, LA Boatner, and RG Wilson. Ferromagnetism in mn-implanted zno: Sn single crystals. *Applied Physics Letters*, 82(2):239–241, 2003.

[13] DP Norton, ME Overberg, SJ Pearton, K Pruessner, JD Budai, LA Boatner, MF Chisholm, JS Lee, ZG Khim, YD Park, et al. Ferromagnetism in cobalt-implanted zno. *Applied Physics Letters*, 83(26):5488–5490, 2003.

[14] Marcus W. Doherty, Neil B. Manson, Paul Delaney, Fedor Jelezko, Joerg Wrachtrup, and Lloyd C. L. Hollenberg. The nitrogen-vacancy colour centre in diamond. *PHYSICS REPORTS-REVIEW SECTION OF PHYSICS LETTERS*, 528(1):1–45, JUL 1 2013.

[15] Romana Schirhagl, Kevin Chang, Michael Loretz, and Christian L. Degen. Nitrogen-Vacancy Centers in Diamond: Nanoscale Sensors for Physics and Biology. In Johnson, MA and Martinez, TJ, editor, *ANNUAL REVIEW OF PHYSICAL CHEMISTRY, VOL 65*, volume 65 of *Annual Review of Physical Chemistry*, pages 83–105. ANNUAL REVIEWS, 4139 EL CAMINO WAY, PO BOX 10139, PALO ALTO, CA 94303-0897 USA, 2014.

[16] J. R. Weber, W. F. Koehl, J. B. Varley, A. Janotti, B. B. Buckley, C. G. Van de Walle, and D. D. Awschalom. Quantum computing with defects. *PROCEEDINGS OF THE NATIONAL ACADEMY OF SCIENCES OF THE UNITED STATES OF AMERICA*, 107(19):8513–8518, MAY 11 2010.

[17] David J. Christle, Abram L. Falk, Paolo Andrich, Paul V. Klimov, Jawad Ul Hassan, Nguyen T. Son, Erik Janzén, Takeshi Ohshima, and David D. Awschalom. Isolated electron spins in silicon carbide with millisecond coherence times. *Nature Materials*, 14(2):160–163, feb 2015.

[18] Matthias Widmann, Sang-Yun Lee, Torsten Rendler, Nguyen Tien Son, Helmut Fedder, Seoyoung Paik, Li-Ping Yang, Nan Zhao, Sen Yang, Ian Booker, Andrej Denisenko, Mohammad Jamali, Seyed Ali Momenzadeh, Ilja Gerhardt, Takeshi Ohshima, Adam Gali, Erik Janzén, and Jörg Wrachtrup. Coherent control of single spins in silicon carbide at room temperature. *Nature Materials*, 14(2):164–168, feb 2015.

[19] S Castelletto, B C Johnson, V Ivády, N Stavrias, T Umeda, A Gali, and T Ohshima. A silicon carbide room-temperature single-photon source. *Nature Materials*, 13(2):151–156, feb 2014.

[20] T. Schenkel, C. D. Weis, C. C. Lo, A. Persaud, I. Chakarov, D. H. Schneider, and J. Bokor. Deterministic doping and the exploration of spin qubits. *AIP Conference Proceedings*, 1640(1):124–128, 2015.

[21] David N. Jamieson, William I.L. Lawrie, Simon G. Robson, Alexander M. Jakob, Brett C. Johnson, and Jeffrey C. McCallum. Deterministic doping. *Materials Science in Semiconductor Processing*, 62:23 – 30, 2017. Advanced doping methods in semiconductor devices and nanostructures.

[22] Cihan Sahin, Philipp Geppert, Andreas Müllers, and Herwig Ott. A high repetition deterministic single ion source. *New Journal of Physics*, 19(12):123005, 2017.

[23] D. N. Jamieson, W. I. L. Lawrie, F. E. Hudson, A. S. Dzurak, A. Morello, S. G. Robson, A. M. Jakob, B. C. Johnson, and J. C. McCallum. Deterministic atom placement by ion implantation: Few and single atom devices for quantum computer technology. In *2016 21st International Conference on Ion Implantation Technology (IIT)*, pages 1–6, Sept 2016.

[24] Jessica Van Donkelaar, C Yang, ADC Alves, JC McCallum, C Hougaard, BC Johnson, FE Hudson, AS Dzurak, A Morello, D Spemann, et al. Single atom devices by ion implantation. *Journal of Physics: Condensed Matter*, 27(15):154204, 2015.

[25] C. Mechri, P. Ruello, J. M. Breteau, M. R. Baklanov, P. Verdonck, and V. Gusev. Depth-profiling of elastic inhomogeneities in transparent nanoporous low-k materials by picosecond ultrasonic interferometry. *Appl. Phys. Lett.*, 95(9):091907, aug 2009.

[26] V. Gusev, A. M. Lomonosov, P. Ruello, A. Ayouch, and G. Vaudel. Depth-profiling of elastic and optical inhomogeneities in transparent materials by picosecond ultrasonic interferometry: Theory. *J. Appl. Phys.*, 110(12):124908, dec 2011.

[27] Alexey M Lomonosov, Adil Ayouch, Pascal Ruello, Gwenaelle Vaudel, Mikhail R Baklanov, Patrick Verdonck, Larry Zhao, and Vitalyi E. Gusev. Nanoscale Noncontact Subsurface Investigations of Mechanical and Optical Properties of Nanoporous Low- k Material Thin Film. *ACS Nano*, 6(2):1410, feb 2012.

[28] G. Tas, J. J. Loomis, H. J. Maris, A. A. Bailes, and L. E. Seiberling. Picosecond ultrasonics study of the modification of interfacial bonding by ion implantation. *Appl. Phys. Lett.*, 72(18):2235, 1998.

[29] Sergey M. Nikitin, Nikolay Chigarev, Vincent Tournat, Alain Bulou, Damien Gasteau, Bernard Castagnede, Andreas Zerr, and Vitalyi E. Gusev. Revealing sub-μm and μm-scale textures in H2O ice at megabar pressures by time-domain Brillouin scattering. *Sci. Rep.*, 5(1):9352, aug 2015.

[30] Maju Kuriakose, Samuel Raetz, Nikolay Chigarev, Sergey M. Nikitin, Alain Bulou, Damien Gasteau, Vincent Tournat, Bernard Castagnede, Andreas Zerr, and Vitalyi E. Gusev. Picosecond laser ultrasonics for imaging of transparent polycrystalline materials compressed to megabar pressures. *Ultrasonics*, 69:259, jul 2016.

[31] F. Hudert, A. Bartels, T. Dekorsy, and K. Köhler. Influence of doping profiles on coherent acoustic phonon detection and generation in semiconductors. *J. Appl. Phys.*, 104:123509, 2008.

[32] J. Dai, P. Mukundhan, C. Kim, and H. J. Maris. Analysis of a picosecond ultrasonic method for measurement of stress in a substrate. *Journal of Applied Physics*, 119(10):105705, mar 2016.

[33] M. Khafizov, J. Pakarinen, L. He, H.B. Henderson, M.V. Manuel, A.T. Nelson, B.J. Jaques, D.P. Butt, and D.H. Hurley. Subsurface imaging of grain microstructure using picosecond ultrasonics. *Acta Mater.*, 112:209, jun 2016.

[34] I. Chaban, D. Shin, C. Klieber, R. Busselez, V. Gusev, Keith A. Nelson, and T. Pezeril. Time-domain Brillouin scattering for the determination of laser-induced temperature gradients in liquids. *Rev. Sci. Instrum.*, 88:074904, feb 2017.

[35] A. Steigerwald, Y. Xu, J. Qi, J. Gregory, X. Liu, J. K. Furdyna, K. Varga, a. B. Hmelo, G. Lupke, L. C. Feldman, and N. Tolk. Semiconductor point defect concentration profiles measured using coherent acoustic phonon waves. *Appl. Phys. Lett.*, 94(11):111910, mar 2009.

[36] Justin Gregory, Andrew Steigerwald, Hiroaki Takahashi, Anthony Hmelo, and Norman Tolk. Ion implantation induced modification of optical properties in single-crystal diamond studied by coherent acoustic phonon spectroscopy. *Appl. Phys. Lett.*, 101(18):181904, oct 2012.

[37] M. J. A. Schuetz, E. M. Kessler, G. Giedke, L. M. K. Vandersypen, M. D. Lukin, and J. I. Cirac. Universal quantum transducers based on surface acoustic waves. *Phys. Rev. X*, 5:031031, Sep 2015.

[38] D G Ashworth, R Oven, and B Mundin. Representation of ion implantation profiles by Pearson frequency distribution curves. *Journal of Physics D: Applied Physics*, 23(7):870–876, jul 1990.

[39] F. JAHANSHAH, K. SOPIAN, H. ABDULLAH, I. AHMAD, and M. Y. OTHMAN. Investigation On Ion Implantation Mo dels Impact On I-V Curve And Thin Film Solar Cell Efficiency. In *Proceedings of the 7th WSEAS International Conference on Wavelet Analysis & Multirate Systems*, pages 133–137, Arcachon, 2007.

[40] Robert G. Wilson. The pearson iv distribution and its application to ion implanted depth profiles. *Radiation Effects*, 46(3-4):141–147, 1980.

[41] James F. Ziegler, M.D. Ziegler, and J.P. Biersack. {SRIM} the stopping and range of ions in matter (2010). *Nucl. Instrum. Methods Phys. Res., Sect. B*, 268(1112):1818, jun 2010.

[42] B. C. Daly, T. B. Norris, J. Chen, and J. B. Khurgin. Picosecond acoustic phonon pulse propagation in silicon. *Physical Review B*, 70(21):214307, dec 2004.

[43] Saori Kashiwada, Osamu Matsuda, Jeremy J. Baumberg, Roberto Li Voti, and Oliver B. Wright. In situ monitoring of the growth of ice films by laser picosecond acoustics. *Journal of Applied Physics*, 100(7):073506, 2006.

[44] O. Matsuda, O. B. Wright, D. H. Hurley, V. Gusev, and K. Shimizu. Coherent shear phonon generation and detection with picosecond laser acoustics. *Phys. Rev. B*, 77:224110, Jun 2008.

[45] Guray Tas and Humphrey J. Maris. Electron diffusion in metals studied by picosecond ultrasonics. *Phys. Rev. B*, 49:15046–15054, Jun 1994.

[46] Sabrina Sadtler, Arnaud Devos, and Marie Foret. Hypersound damping in vitreous silica measured by ultrafast acoustics. *International Journal of Thermophysics*, 34(8):1785–1794, Sep 2013.

[47] J. K. Miller, J. Qi, Y. Xu, Y.-J. Cho, X. Liu, J. K. Furdyna, I. Perakis, T. V. Shahbazyan, and N. Tolk. Near-bandgap wavelength dependence of long-lived traveling coherent longitudinal acoustic phonons in GaSb-GaAs heterostructures. *Physical Review B*, 74(11):113313, sep 2006.

[48] S. Wu, P. Geiser, J. Jun, J. Karpinski, and Roman Sobolewski. Femtosecond optical generation and detection of coherent acoustic phonons in GaN single crystals. *Physical Review B*, 76(8):085210, aug 2007.

[49] Andrey Baydin, Halina Krzyzanowska, Munthala Dhanunjaya, S. V. S. Nageswara Rao, Jimmy L. Davidson, Leonard C. Feldman, and Norman H. Tolk. Depth dependent modification of optical constants arising from H+ implantation in n-type 4H-SiC measured using coherent acoustic phonons. *APL Photonics*, 1(3):036102, jun 2016.

[50] Andrey Baydin, Halina Krzyzanowska, Rustam Gatamov, Joy Garnett, and Norman Tolk. The photoelastic coefficient P 12 of H+ implanted GaAs as a function of defect density. *Scientific Reports*, 7(1):15150, dec 2017.

[51] O. B. Wright. Thickness and sound velocity measurement in thin transparent films with laser picosecond acoustics. *Journal of Applied Physics*, 71(4):1617–1629, feb 1992.

[52] Jacqueline Vollmann, Dieter M. Profunser, and Jürg Dual. Sensitivity improvement of a pumpprobe set-up for thin film and microstructure metrology. *Ultrasonics*, 40(1-8):757–763, may 2002.

[53] C. W. Hsu, R. P. Huang, J. Chen, J Tan, H. F. Huang, Welch Lin, Y L Hsieh, W C Tsao, C H Chen, Y. M. Lin, C H Lin, H K Hsu, K Liu, C C Huang, J Y Wu, J Dai, and P. Mukundhan. In-line high-K/metal gate monitoring using picosecond ultrasonics. volume 8681, page 86811C, apr 2013.

[54] L.L. Chapelon, J Vitiello, D Neira, J Torres, J.C. Royer, D Barbier, F Naudin, G Tas, P Mukundhan, and J Clerico. Measuring the Young's modulus of ultralow-k mate-

rials with the non destructive picosecond ultrasonic method. *Microelectronic Engineering*, 83(11-12):2346–2350, nov 2006.

[55] Guray Tas and Humphrey J. Maris. Electron diffusion in metals studied by picosecond ultrasonics. *Physical Review B*, 49(21):15046–15054, jun 1994.

[56] O B Wright, B Perrin, O Matsuda, and V E Gusev. Ultrafast carrier diffusion in gallium arsenide probed with picosecond acoustic pulses. *Physical Review B*, 64(8):081202, aug 2001.

[57] T. Saito, O. Matsuda, and O. B. Wright. Picosecond acoustic phonon pulse generation in nickel and chromium. *Physical Review B*, 67(20):205421, may 2003.

[58] E. S K Young, a. V. Akimov, R. P. Campion, a. J. Kent, and V. Gusev. Picosecond strain pulses generated by a supersonically expanding electron-hole plasma in GaAs. *Physical Review B - Condensed Matter and Materials Physics*, 86(15):1–13, 2012.

[59] A. V. Akimov, A. V. Scherbakov, D. R. Yakovlev, C. T. Foxon, and M. Bayer. Ultrafast band-gap shift induced by a strain pulse in semiconductor heterostructures. *Phys. Rev. Lett.*, 97:037401, Jul 2006.

[60] Andrey V. Akimov, Alexey V. Scherbakov, Dmitri R. Yakovlev, Manfred Bayer, and Anthony Kent. Optical and photocurrent spectroscopy with picosecond strain pulses. *Journal of Luminescence*, 131(3):404–408, mar 2011.

[61] C. Brüggemann, A. V. Akimov, A. V. Scherbakov, M. Bombeck, C. Schneider, S. Höfling, A. Forchel, D. R. Yakovlev, and M. Bayer. Laser mode feeding by shaking quantum dots in a planar microcavity. *Nature Photonics*, 6(1):30–34, jan 2012.

[62] Thomas Czerniuk, Daniel Wigger, A. V. Akimov, Christian Schneider, M. Kamp, S. Höfling, D. R. Yakovlev, Tilmann Kuhn, D. E. Reiter, and Manfred Bayer. Picosecond Control of Quantum Dot Laser Emission by Coherent Phonons. *Physical Review Letters*, 118(13):133901, mar 2017.

[63] H. N. Lin, R. J. Stoner, H. J. Maris, and J. Tauc. Phonon attenuation and velocity measurements in transparent materials by picosecond acoustic interferometry. *Journal of Applied Physics*, 69(7):3816–3822, apr 1991.

[64] Wei Chen, Humphrey J. Maris, Zbigniew R. Wasilewski, and Shin-Ichiro Tamura. Attenuation and velocity of 56 GHz longitudinal phonons in gallium arsenide from 50 to 300 K. *Philosophical Magazine Part B*, 70(3):687–698, sep 1994.

[65] P. Emery and A. Devos. Acoustic attenuation measurements in transparent materials in the hypersonic range by picosecond ultrasonics. *Applied Physics Letters*, 89(19):191904, nov 2006.

[66] Brian C Daly, Kwangu Kang, and David G Cahill. Attenuation of picosecond ultrasonic pulses in a thin silicon wafer. In *1st Int. Symposium on Laser Ultrasonics: Science, Technology and Applications*, 2008.

[67] B. C. Daly, K. Kang, Y. Wang, and David G. Cahill. Picosecond ultrasonic measurements of attenuation of longitudinal acoustic phonons in silicon. *Physical Review B*, 80(17):174112, nov 2009.

[68] Juerg Bryner, Timothy Kehoe, Jacqueline Vollmann, Laurent Aebi, Ingo Wenke, and Jurg Dual. Phonon attenuation in the GHz regime: Measurements and simulations with a visco-elastic material model. *Physics Procedia*, 3(1):343–350, jan 2010.

[69] H.Y. Hao, W. Singhsomroje, and H.J. Maris. Studies of soliton formation of longitudinal acoustic phonons in crystalline solids. *Physica B: Condensed Matter*, 316-317:147–149, may 2002.

[70] A V Akimov, A V Scherbakov, P J S van Capel, J I Dijkhuis, T Berstermann, D R Yakovlev, and M Bayer. Acoustic solitons in semiconductor nanostructures. *Journal of Physics: Conference Series*, 92:012002, dec 2007.

[71] P. J. S. van Capel and J. I. Dijkhuis. Time-resolved interferometric detection of ultrashort strain solitons in sapphire. *Physical Review B*, 81(14):144106, apr 2010.

[72] Vitalyi E. Gusev. Detection of nonlinear picosecond acoustic pulses by time-resolved Brillouin scattering. *Journal of Applied Physics*, 116(6):064907, 2014.

[73] Christoph Klieber, Vitalyi E. Gusev, Thomas Pezeril, and Keith A. Nelson. Nonlinear acoustics at GHz frequencies in a viscoelastic fragile glass former. *Physical Review Letters*, 114(6):1–5, 2015.

[74] P.J.S. van Capel, E. Péronne, and J.I. Dijkhuis. Nonlinear ultrafast acoustics at the nano scale. *Ultrasonics*, 56:36–51, feb 2015.

[75] Fernando Pérez-Cota, Richard J Smith, Emilia Moradi, Leonel Marques, Kevin F Webb, and Matt Clark. Thin-film optoacoustic transducers for subcellular brillouin oscillation imaging of individual biological cells. *Applied optics*, 54(28):8388–8398, 2015.

[76] Fernando Perez-Cota, Richard J Smith, Emilia Moradi, K Webb, and Matt Clark. Thin-film transducers for the detection and imaging of brillouin oscillations in transmission on cultured cells. In *Journal of Physics: Conference Series*, volume 684, page 012003. IOP Publishing, 2016.

[77] Ryan Beardsley, Andrey V Akimov, Jake DG Greener, Garry W Mudd, Sathyan Sandeep, Zakhar R Kudrynskyi, Zakhar D Kovalyuk, Amalia Patanè, and Anthony J Kent. Nanomechanical probing of the layer/substrate interface of an exfoliated inse sheet on sapphire. *Scientific reports*, 6:26970, 2016.

[78] Martin Grossmann, Martin Schubert, Chuan He, Delia Brick, Elke Scheer, Mike Hettich, Vitalyi Gusev, and Thomas Dekorsy. Characterization of thin-film adhesion and phonon lifetimes in Al/Si membranes by picosecond ultrasonics. *New Journal of Physics*, 19(5):053019, may 2017.

[79] Maroun Abi Ghanem, Thomas Dehoux, Liwang Liu, Guillaume Le Saux, Laurent Plawinski, Marie-Christine Durrieu, and Bertrand Audoin. Opto-acoustic microscopy reveals adhesion mechanics of single cells. *Review of Scientific Instruments*, 89(1):014901, 2018.

[80] I-Ju Chen, Pierre-Adrien Mante, Cheng-Kai Chang, Szu-Chi Yang, Hui-Yuan Chen, Yu-Ru Huang, Li-Chyong Chen, Kuei-Hsien Chen, Vitalyi Gusev, and Chi-Kuang Sun. Graphene-to-Substrate Energy Transfer through Out-of-Plane Longitudinal Acoustic Phonons. *Nano Letters*, 14(3):1317–1323, mar 2014.

[81] Vasily V. Temnov. Ultrafast acousto-magneto-plasmonics. *Nature Photonics*, 6(11):728–736, nov 2012.

[82] Oleksandr Kovalenko, Thomas Pezeril, and Vasily V. Temnov. New Concept for Magnetization Switching by Ultrafast Acoustic Pulses. *Physical Review Letters*, 110(26):266602, jun 2013.

[83] O. Kovalenko, V. Shalagatskyi, T. Pezeril, V. Gusev, D. Makarov, and V. V. Temnov. Picosecond Strain Pulses for Ultrafast Magnetoacoustics. In *Proceedings of the International Conference UMC 2013*, pages 248–250. 2015.

[84] Vasily V. Temnov, Ilya Razdolski, Thomas Pezeril, Denys Makarov, Denis Seletskiy, Alexey Melnikov, and Keith A. Nelson. Towards the nonlinear acousto-magneto-plasmonics. *Journal of Optics*, 18(9):093002, sep 2016.

[85] Evan J. Reed, Michael R. Armstrong, Ki Yong Kim, and James H. Glownia. Atomic-scale time and space resolution of terahertz frequency acoustic waves. *Physical Review Letters*, 101(1):1–4, 2008.

[86] Michael R. Armstrong, Evan J. Reed, Ki-Yong Kim, James H. Glownia, William M. Howard, Edwin L. Piner, and John C. Roberts. Observation of terahertz radiation coherently generated by acoustic waves. *Nature Physics*, 5(4):285–288, apr 2009.

[87] Bolin Liao, A. A. Maznev, Keith A. Nelson, and Gang Chen. Photo-excited charge carriers suppress sub-terahertz phonon mode in silicon at room temperature. *Nature Communications*, 7:13174, oct 2016.

[88] Osamu Matsuda, Maria Cristina Larciprete, Roberto Li Voti, and Oliver B. Wright. Fundamentals of picosecond laser ultrasonics. *Ultrasonics*, 56:3, feb 2015.

[89] Pascal Ruello and Vitalyi E. Gusev. Physical mechanisms of coherent acoustic phonons generation by ultrafast laser action. *Ultrasonics*, 56:21, 2015.

[90] T. Saito, O. Matsuda, and O. B. Wright. Picosecond acoustic phonon pulse generation in nickel and chromium. *Phys. Rev. B*, 67:205421, May 2003.

[91] O. Matsuda and O. B. Wright. Reflection and transmission of light in multilayers perturbed by picosecond strain pulse propagation. *Journal of the Optical Society of America B*, 19(12):3028, dec 2002.

[92] O Matsuda and O.B Wright. Laser picosecond acoustics in a two-layer structure with oblique probe light incidence. *Ultrasonics*, 42(1-9):653–656, apr 2004.

[93] J. Bardeen and W. Shockley. Deformation potentials and mobilities in non-polar crystals. *Phys. Rev.*, 80:72–80, Oct 1950.

[94] Sadao Adachi. Model dielectric constants of gap, gaas, gasb, inp, inas, and insb. *Phys. Rev. B*, 35:7454–7463, May 1987.

[95] Sadao Adachi. Model dielectric constants of si and ge. *Phys. Rev. B*, 38:12966–12976, Dec 1988.

[96] M. R. Lorenz, G. D. Pettit, and R. C. Taylor. Band gap of gallium phosphide from 0 to 900°k and light emission from diodes at high temperatures. *Phys. Rev.*, 171:876–881, Jul 1968.

[97] Guoqing Chang, Charles J. Divin, Jun Yang, Malakeh A Musheinish, Steven L. Williamson, Almantas Galvanauskas, and Theodore B. Norris. Gap waveguide emitters for high power broadband thz generation pumped by yb-doped fiber lasers. *Opt. Express*, 15(25):16308–16315, Dec 2007.

[98] Jiang Li, Lu Chai, Junkai Shi, Bowen Liu, Baozhong Xu, Minglie Hu, Yanfeng Li, Qirong Xing, Chingyue Wang, Andrey B. Fedotov, and Aleksei M. Zheltikov. Efficient terahertz wave generation from gap crystals pumped by chirp-controlled

pulses from femtosecond photonic crystal fiber amplifier. *Applied Physics Letters*, 104(3):031117, 2014.

[99] Katsuyoshi Aoki, Janne Savolainen, and Martina Havenith. Broadband terahertz pulse generation by optical rectification in gap crystals. *Applied Physics Letters*, 110(20):201103, 2017.

[100] J.-P. Negel, R. Hegenbarth, A. Steinmann, B. Metzger, F. Hoos, and H. Giessen. Compact and cost-effective scheme for thz generation via optical rectification in gap and gaas using novel fs laser oscillators. *Applied Physics B*, 103(1):45–50, Apr 2011.

[101] Kyosuke Saito, Tadao Tanabe, Yutaka Oyama, Ken Suto, and Jun ichi Nishizawa. Terahertz-wave generation by gap rib waveguides via collinear phase-matched difference-frequency mixing of near-infrared lasers. *Journal of Applied Physics*, 105(6):063102, 2009.

[102] Takeo Takizawa. Wavelength modulated reflectivities of the direct exciton edge in gap. *Journal of the Physical Society of Japan*, 52(3):1057–1063, 1983.

[103] Manuel Cardona and Niels E. Christensen. Acoustic deformation potentials and heterostructure band offsets in semiconductors. *Phys. Rev. B*, 35:6182–6194, Apr 1987.

[104] O. Madelung, U. Rössler, and M. Schulz, editors. *Gallium phosphide (GaP), band structure*, pages 1–6. Springer Berlin Heidelberg, Berlin, Heidelberg, 2002.

[105] HM Lawler, A Steigerwald, J Gregory, H Krzyzanowska, and NH Tolk. Experimental and theoretical determination of the opto-acoustic spectrum of silicon. *Materials Research Express*, 1(2):025701, 2014.

[106] Pierre-Adrien Mante, Constantinos C Stoumpos, Mercouri G Kanatzidis, and Arkady Yartsev. Electron–acoustic phonon coupling in single crystal ch 3 nh 3 pbi 3 perovskites revealed by coherent acoustic phonons. *Nature communications*, 8:14398, 2017.

[107] Louis Tirino, Michael Weber, Kevin F Brennan, and Enrico Bellotti. A general monte carlo model including the effect of the acoustic deformation potential on the transport properties. *Journal of Computational Electronics*, 3(2):81–93, 2004.

[108] Sarit Dhar, S.T. Pantelides, L.C. Feldman, Shurui Wang, T. Isaacs-Smith, and J.R. Williams. Interface passivation of Silicon Dioxide layers on Silicon Carbide. In *2005 International Semiconductor Device Research Symposium*, volume 30, pages 236–237. IEEE, apr 2005.

[109] M. S. Janson, M. K. Linnarsson, A. Hallen, B. G. Svensson, N. Achtziger, L. Uneus, A. Lloyd Spetz, and U. Forsberg. Hydrogen in the Wide Bandgap Semiconductor Silicon Carbide. *Physica Scripta*, page 99, 2004.

[110] G. Alfieri, E. V. Monakhov, B. G. Svensson, and A. Hallén. Defect energy levels in hydrogen-implanted and electron-irradiated n-type 4H silicon carbide. *Journal of Applied Physics*, 98(11):113524, dec 2005.

[111] Giovanni Alfieri and Tsunenobu Kimoto. Deep level transient spectroscopy study of defects in hydrogen implanted p-type 4HSiC. *Journal of Applied Physics*, 101(10):103716, may 2007.

[112] G. Alfieri and T. Kimoto. Evidence for a hydrogen-related defect in implanted p-type 4H-SiC. *New Journal of Physics*, 10(7):073017, jul 2008.

[113] A. Barcz, M. Kozubal, R. Jakieła, J. Ratajczak, J. Dyczewski, K. Gołaszewska, T. Wojciechowski, and G. K. Celler. Diffusion and impurity segregation in hydrogen-implanted silicon carbide. *Journal of Applied Physics*, 115(22):223710, jun 2014.

[114] V. P. Amarasinghe, L. Wielunski, A. Barcz, L. C. Feldman, and G. K. Celler. Properties of H+ Implanted 4H-SiC as Related to Exfoliation of Thin Crystalline Films. *ECS Journal of Solid State Science and Technology*, 3(3):P37–P42, jan 2014.

[115] C Thomsen, HT T Grahn, HJ J Maris, and J Tauc. Surface generation and detection of phonons by picosecond light pulses. *Phys. Rev. B*, 34(6):4129, sep 1986.

[116] R. Ahuja, A. Ferreira da Silva, C. Persson, J. M. Osorio-Guillén, I. Pepe, K. Järrendahl, O. P A Lindquist, N. V. Edwards, Q. Wahab, and B. Johansson. Optical properties of 4HSiC. *Journal of Applied Physics*, 91(4):2099–2103, feb 2002.

[117] D.B. Hondongwa, L.R. Olasov, B.C. Daly, S.W. King, and J. Bielefeld. Thermal conductivity and sound velocity measurements of plasma enhanced chemical vapor deposited a-SiC:H thin films. *Thin Solid Films*, 519(22):7895–7898, sep 2011.

[118] I. R. CoxSmith, H. C. Liang, and R. O. Dillon. Sound velocity in amorphous films of germanium and silicon. *Journal of Vacuum Science & Technology A: Vacuum, Surfaces, and Films*, 3(3):674–677, may 1985.

[119] Alfio Battiato, Federico Bosia, Simone Ferrari, Paolo Olivero, Anna Sytchkova, and Ettore Vittone. Spectroscopic measurement of the refractive index of ion-implanted diamond. *Optics Letters*, 37(4):671, feb 2012.

[120] David T. Y. Wei, William W. Lee, and Louis R. Bloom. Large refractive index change induced by ion implantation in lithium niobate. *Applied Physics Letters*, 25(6):329–331, sep 1974.

[121] K. Wenzlik, J. Heibei, and E. Voges. Refractive index profiles of helium implanted LiNbO3 and LiTaO3. *Physica Status Solidi (a)*, 61(2):K207–K211, oct 1980.

[122] T. C. Sum, a. a. Bettiol, J. A. van Kan, S. Venugopal Rao, F. Watt, K. Liu, and E. Y B Pun. Direct imaging of the end-of-range and surface profiles of proton-beam written erbium-doped waveguide amplifiers by atomic force microscopy. *Journal of Applied Physics*, 98(3):033533, aug 2005.

[123] In Tae Bae, William J. Weber, and Yanwen Zhang. Direct measurement of local volume change in ion-irradiated and annealed SiC. *Journal of Applied Physics*, 106(12):1–5, 2009.

[124] W. Jiang, C. M. Wang, W. J. Weber, M. H. Engelhard, and L. V. Saraf. Direct determination of volume changes in ion-beam-irradiated SiC. *Journal of Applied Physics*, 95(9):4687–4690, may 2004.

[125] R. L. Hines. Radiation Damage of Diamond by 20-keV Carbon Ions. *Physical Review*, 138(6A):A1747–A1751, jun 1965.

[126] P. Olivero, S. Calusi, L. Giuntini, S. Lagomarsino, A. Lo Giudice, M. Massi, S. Sciortino, M. Vannoni, and E. Vittone. Controlled variation of the refractive index in ion-damaged diamond. *Diamond and Related Materials*, 19(5-6):428–431, may 2010.

[127] M. a. Draganski, E. Finkman, B. C. Gibson, B. a. Fairchild, K. Ganesan, N. Nabatova-Gabain, S. Tomljenovic-Hanic, a. D. Greentree, and S. Prawer. Tailoring the optical constants of diamond by ion implantation. *Optical Materials Express*, 2(5):644, may 2012.

[128] S Lagomarsino, P Olivero, S Calusi, D Gatto Monticone, L Giuntini, M Massi, S Sciortino, A Sytchkova, A Sordini, and M Vannoni. Complex refractive index variation in proton-damaged diamond. *Optics Express*, 20(17):19382, aug 2012.

[129] G. K. Hubler, C. N. Waddell, W. G. Spitzer, J. E. Fredrickson, S. Prussin, and R. G. Wilson. Highfluence implantations of silicon: Layer thickness and refractive indices. *Journal of Applied Physics*, 50(5):3294–3303, may 1979.

[130] G. K. Hubler, P. R. Malmberg, C. A. Carosella, T. P. Smith, W. G. Spitzer, C. N. Waddell, and C. N. Phillippi. Optical effects resulting from deep implants of silicon with nitrogen and phosphorus. *Radiation Effects*, 48(1-4):81–85, jan 1980.

[131] C. N. Waddell, W. G. Spitzer, G. K. Hubler, and J. E. Fredrickson. Infrared studies of isothermal annealing of ionimplanted silicon: Refractive indices, regrowth rates, and carrier profiles. *Journal of Applied Physics*, 53(8):5851–5862, aug 1982.

[132] J. E. Fredrickson, C. N. Waddell, W. G. Spitzer, and G. K. Hubler. Effects of thermal annealing on the refractive index of amorphous silicon produced by ion implantation. *Applied Physics Letters*, 40(2):172–174, jan 1982.

[133] Kou-Wei Wang, William G. Spitzer, Graham K. Hubler, and Edward P. Donovan.

Effect of annealing on the optical properties of ionimplanted Ge. *Journal of Applied Physics*, 57(8):2739–2751, apr 1985.

[134] A S Pine. *Brillouin Scattering in Semiconductors*. Springer Berlin Heidelberg, 1975.

[135] S. Adachi. *Elastooptic and electrooptic effects*. World Scietific, oct 1994.

[136] Jasper Chan, Amir H. Safavi-Naeini, Jeff T. Hill, Seán Meenehan, and Oskar Painter. Optimized optomechanical crystal cavity with acoustic radiation shield. *Appl. Phys. Lett.*, 101(8):081115, aug 2012.

[137] Krishna C. Balram, Marcelo Davanço, Ju Young Lim, Jin Dong Song, and Kartik Srinivasan. Moving boundary and photoelastic coupling in GaAs optomechanical resonators. *Optica*, 1(6):414, dec 2014.

[138] P. Renosi, J. Sapriel, and B. Djafari-Rouhani. Resonant acousto-optic effects in InP and GaAs and related devices. In *5th International Conference on Indium Phosphide and Related Materials*, pages 592–595. IEEE, 1993.

[139] W. Schimmerling and S.B. Curtis. Workshop on the radiation environment of the satellite power system. Lawrence Berkeley National Laboratory, 1978.

[140] A.H. Johnston and B.G. Rax. Proton damage in linear and digital optocouplers. *IEEE Trans. Nucl. Sci.*, 47(3):675, jun 2000.

[141] SÉbastien Bourdarie and Michael Xapsos. The near-earth space radiation environment. *IEEE Trans. Nucl. Sci.*, 55(4):1810, aug 2008.

[142] H.-Y. Hao and H. Maris. Dispersion of the long-wavelength phonons in Ge, Si, GaAs, quartz, and sapphire. *Phys. Rev. B*, 63(22):224301, 2001.

[143] C. Rossignol, J.M. Rampnoux, T. Dehoux, S. Dilhaire, and B. Audoin. Picosecond ultrasonics time resolved spectroscopy using a photonic crystal fiber. *Ultrasonics*, 44(SUPPL.):e1283, dec 2006.

[144] Emmanuel Péronne and Bernard Perrin. Generation and detection of acoustic solitons in crystalline slabs by laser ultrasonics. *Ultrasonics*, 44:e1203, 2006.

[145] a V Scherbakov, M Bombeck, J V Jäger, a S Salasyuk, T L Linnik, V E Gusev, D R Yakovlev, a V Akimov, and M Bayer. Picosecond opto-acoustic interferometry and polarimetry in high-index GaAs. *Opt. Express*, 21(14):16473, 2013.

[146] Chuan He, Oliver Ristow, Martin Grossmann, Delia Brick, Yuning Guo, Martin Schubert, Mike Hettich, Vitalyi Gusev, and Thomas Dekorsy. Acoustic waves undetectable by transient reflectivity measurements. *Phys. Rev. B*, 95(18):184302, may 2017.